Coexistence of multiple long-time solutions for two-dimensional laminar flow past a linearly sprung circular cylinder with a rotational nonlinear energy sink

Antoine B. Blanchard,[1,*] Lawrence A. Bergman,[1] Alexander F. Vakakis,[2] and Arne J. Pearlstein[2,†]

[1]*Department of Aerospace Engineering, University of Illinois at Urbana-Champaign, Urbana, Illinois 61801, USA*

[2]*Department of Mechanical Science and Engineering, University of Illinois at Urbana-Champaign, Urbana, Illinois 61801, USA*

For two-dimensional flow past a linearly sprung circular cylinder to which has been attached an internal "nonlinear energy sink" consisting of a mass allowed to rotate about the cylinder axis and a viscous damper that linearly retards the rotational motion of that mass, we show, for a given set of parameters, that as many as three distinct unsteady long-time solutions (two periodic and one chaotic), in addition to one or more steady solutions, can coexist. For other combinations of the parameters, two unsteady solutions (both periodic, one periodic and one quasiperiodic, one periodic and one chaotic, one quasiperiodic and one chaotic, or both chaotic) can coexist with one or more steady solutions. These multiple solutions, all of which appear to be linearly stable, are found in a range of Reynolds number ($15 < \mathrm{Re} < 50$) in which the flow is expected to be two dimensional. The discovery of this unprecedented degree of solution multiplicity establishes the potential of this system to serve, at low Re, as a test bed for detailed investigation of basins of attraction of the Navier-Stokes equations, and in studies of noise- and disturbance-induced transitions between different long-time solutions.

I. INTRODUCTION

A key issue in understanding the solution structure of the Navier-Stokes equations is the dependence of solutions on initial conditions. One manifestation of this is the sensitive dependence of turbulent (and more generally, temporally chaotic) solutions on initial conditions.

A second facet of this issue concerns situations in which there exist qualitatively distinct long-time attracting solutions, each with its own basin of attraction in the initial condition space. In several cases, such behavior has been characterized, including for von Kármán rotating disk flow and variants [1,2]; vortex-induced vibration in flow past a cylinder [3,4]; flow in a pipe, where steady axisymmetric, fully developed flow can exist over a broad range of Reynolds numbers with either transitional or turbulent flow also being a solution [5]; Rayleigh-Bénard convection [6–9]; Taylor-Couette flow [10–14]; flow in a pair of channels [15]; dynamo-related magnetohydrodynamic flows [16]; multicomponent convection in a porous medium [17]; flow in a nearly symmetric two-dimensional sudden expansion [18]; and a drop rising through an immiscible liquid [19,20].

---

[*]Present address: Massachusetts Institute of Technology, 77 Massachusetts Avenue, Room 5-318, Cambridge, Massachusetts 02139, USA.

[†]Corresponding author: ajp@illinois.edu

Situations having more than one long-time attracting solution (referred to here as "long-time solution") are of interest for three reasons. First, if transition from one long-time solution to another can be induced by an intentional disturbance, then "switching" from one flow state to another has the potential to favorably affect heat or mass transfer, aerodynamic performance, or chemical reaction rates in a controllable way. Second, systems in which there are coexisting long-time solutions facilitate study of transitions induced by underlying thermodynamic [21] or environmental [22] fluctuations. Finally, such situations provide a platform for delineating basins of attraction in the initial condition space.

Identification of multiple long-time solutions typically involves conducting a bifurcation analysis or conducting laboratory or computational experiments to explore the infinite-dimensional space of initial conditions. As a result, there is an interest in systems for which multiplicity occurs in two-dimensional flows at relatively low Reynolds number and quantitative experiments and high-fidelity computations can be performed relatively easily. Two-dimensionality is important from the standpoint of reducing the dimension of the initial condition space. Two-dimensionality and low Reynolds number are important from the standpoint of simplifying experimental measurements and computations, and allowing them to be performed at high resolution.

A particularly attractive class of two-dimensional flows in which to study multiplicity is vortex-induced vibration (VIV) of a linearly sprung circular cylinder, for the case in which cylinder motion is perpendicular to the mean flow. In this case, at a Reynolds number of 100 (based on cylinder diameter), Navrose and Mittal [3,4] recently found a new region of multiplicity in the interior of the lock-in region, in addition to the multiplicity previously identified at the "ends" of the lock-in region. Those authors found that the extent of this "middle" range of multiplicity (measured in terms of a dimensionless "reduced speed" defined by the free-stream velocity divided by the product of the cylinder diameter and the *in vacuo* natural frequency of the spring-mass system) decreased linearly to zero as the ratio of cylinder density to fluid density approached ten from above.

Here, we consider multiplicity in a related system previously investigated by Tumkur *et al.* [23], in which two-dimensional flow of an incompressible Newtonian fluid excites cross-stream vibration of a linearly sprung vertical cylinder of circular cross section in an unbounded domain. Inertial coupling between the rectilinear motion of the cylinder and the rotational motion of a mass attached to the cylinder axis, whose rotation is linearly retarded by a damper (e.g., solid-solid friction at the pivot), provides a mechanism for energy to be mechanically dissipated (i.e., not by viscosity within the fluid). As discussed by Tumkur *et al.* [23], the key issues are (a) inertial coupling of the rectilinear and rotational motions, (b) the inherent lack of a natural frequency for the rotational motion (when the attached mass rotates about a vertical axis, there is no preferred frequency associated with gravity), and (c) mechanical dissipation, which combine to give rise to a "nonlinear energy sink" (NES). Gendelman *et al.* [24] and Sigalov *et al.* [25,26] showed that for a linearly sprung mass undergoing rectilinear motion, attached to a second mass whose rotational motion is linearly retarded by a viscous damper, the free response of this *in vacuo* system is quite complex.

In the context of flow-induced vibration, Tumkur *et al.* [23] showed that a rotational NES allows for a much richer response than is found for "standard" (NES-less) VIV. (In the range of Reynolds numbers considered below, we use "standard VIV" to refer to time-periodic two-dimensional flow and time-periodic motion of a linearly sprung cylinder absent an NES [3,4].)

The present work establishes that up to three long-time periodic, quasiperiodic, or temporally chaotic solutions, along with a steady, symmetric, motionless-cylinder solution, can coexist when the motion of a rotational NES is inertially coupled to the rectilinear motion of the cylinder. The range of multiplicity extends well below the critical Reynolds number for flow past a fixed cylinder ($Re_{fixed} \approx 46$). The results pertain to a density ratio of ten, thus facilitating experiments in water and other liquids.
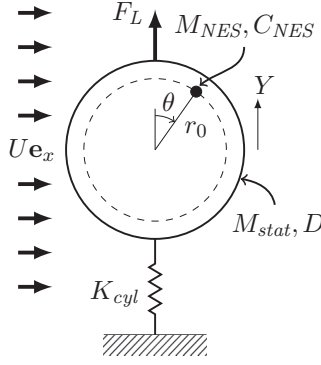
FIG. 1. Linearly sprung cylinder in cross flow with rotational NES.

The remainder of the paper is organized as follows. We present the formulation and computational approach in Sec. II, the results in Secs. III and IV, a discussion in Sec. V, and a conclusion in Sec. VI.

II. FORMULATION AND APPROACH

A. Physical model

The physical problem, involving a Newtonian fluid with constant density ρ_f and kinematic viscosity ν flowing with uniform velocity $U\mathbf{e}_x$ past a linearly sprung circular cylinder with diameter D, is identical to that considered by Tumkur et $al.$ [23], and is shown schematically in Fig. 1. The cylinder is allowed to move transversely to the mean flow, in the y direction, with its motion restrained by a linear spring with spring constant K_{cyl}. The cylinder has an "overall" or "effective" density $\rho_b = (M_{stat} + M_{NES})/(\pi D^2 L/4)$, where L is the spanwise extent of the flow, and M_{stat} and M_{NES} are the masses of the nonrotating part of the cylinder (the "stator") in contact with the flow, and the rotational NES, respectively. (We note that in most laboratory experiments, the spring or other elastic restraint lies outside the span of the flow. Here, the stator, the NES, or both can extend beyond the span of the flow.) The NES consists of two components. First, a mass M_{NES} is allowed to rotate at an effective distance r_0 from the cylinder axis. (For a point mass or a mass concentrated on a line parallel to the cylinder axis, r_0 is simply the distance from the axis. For any distributed mass, Tumkur et $al.$ [23] showed that $r_0 = R_g^2/R_{cm}$, where R_g and R_{cm} are the radius of gyration and the distance from the center of mass to the axis of rotation, respectively.) The second component is a viscous damper, which retards rotation of the attached NES mass with a torque linearly proportional (with coefficient C_{NES}) to the latter's angular velocity.

The dimensionless equations are identical to those of Tumkur et $al.$ [23], given by

$$\frac{\partial \mathbf{v}}{\partial \tau} + \mathbf{v} \cdot \nabla \mathbf{v} = -\nabla p + \frac{1}{\text{Re}} \nabla^2 \mathbf{v}, \tag{1a}$$

$$\nabla \cdot \mathbf{v} = 0, \tag{1b}$$

$$\frac{d^2 y_1}{d\tau^2} + \left[2\pi \frac{g_n^*}{\text{Re}}\right]^2 y_1 = \varepsilon_p \bar{r}_0 \frac{d}{d\tau}\left[\frac{d\theta}{d\tau}\sin\theta\right] + \frac{2C_L}{\pi m^*}, \tag{2a}$$

$$\frac{d^2\theta}{d\tau^2} + \frac{\zeta}{\text{Re}}\frac{d\theta}{d\tau} = \frac{\sin\theta}{\bar{r}_0}\frac{d^2 y_1}{d\tau^2} \tag{2b}$$

where velocity, time, and length (including cylinder displacement) have been scaled with cylinder diameter D and free-stream velocity U, the Reynolds number is $\text{Re} = UD/\nu$, θ is the angular

position of the NES mass rotating about the cylinder axis, and C_L is the lift coefficient. We take $\theta = 0$ to coincide with the positive y axis. The other dimensionless parameters are $m^* = \rho_b/\rho_f$, the dimensionless *in vacuo* natural frequency $g_n^* = D^2\sqrt{K_{\mathrm{cyl}}/(M_{\mathrm{stat}} + M_{\mathrm{NES}})}/(2\pi\nu)$ of the spring-mass system, $\varepsilon_p = [M_{\mathrm{NES}}/(M_{\mathrm{stat}} + M_{\mathrm{NES}})]/(R_{cm}/R_g)^2$, $\bar{r}_0 = r_0/D$, and a dimensionless damping parameter $\zeta = C_{\mathrm{NES}}D^2/(\nu r_0^2 M_{\mathrm{NES}})$. For a point mass or a concentrated line mass, $\varepsilon_p = M_{\mathrm{NES}}/(M_{\mathrm{stat}} + M_{\mathrm{NES}})$. We note that m^* can be made very large, even when the fluid is a liquid, and that ε_p can be varied over a very wide range, by extending the stator and NES beyond the span of the flow.

In the limit of very high damping of the rotational motion of the attached mass, rotation ceases and the system behaves as would a linearly sprung NES-less cylinder, i.e., with no effect of the rotatable mass. In that limit, the motion (or lack thereof) depends only on the Reynolds number, dimensionless spring constant, and ratio of cylinder density to fluid density.

B. Inlet transients

To explore coexistence of multiple long-time solutions, we used inlet transients symmetric and asymmetric about $y = 0$, rather than searching in the initial condition space. These inlet transients smoothly relax to a uniform inlet condition in finite time, providing a finite-time transition from a prescribed inlet disturbance to uniform inlet flow compatible with a steady, symmetric, motionless-cylinder (SSMC) solution. [If $v_x(x, y, \tau) = v_x(x, -y, \tau)$, $v_y(x, y, \tau) = -v_y(x, -y, \tau)$ and $p(x, y, \tau) = p(x, -y, \tau)$, we refer to the flow as symmetric about $y = 0$. The corresponding vorticity distribution is antisymmetric.] Our approach can be thought of as a variation on persistent inlet excitation [27,28], but with a finite duration, since persistent inlet excitation would not be compatible with an SSMC solution.

Each asymmetric inlet transient $\mathbf{v}(x_{in}, y, \tau) = \mathbf{e}_x v_{x,in}(y, \tau)$ with

$$v_{x,A}(y, \tau; \alpha) = \{1 + \alpha\exp[-(y-1)^2/2]\}\left[1 - \frac{\tau}{25}\right] + \frac{\tau}{25}, \tag{3a}$$

$$v_{x,B}(y, \tau; \beta) = \left(1 + \beta\left\{2\frac{\tanh[(y+36)/30]}{\tanh(12/5)} - 1\right\}\right)\left[1 - \frac{\tau}{25}\right] + \frac{\tau}{25}, \tag{3b}$$

$$v_{x,C}(y, \tau; \gamma) = \left[1 + \gamma\frac{y}{36}\right]\left[1 - \frac{\tau}{25}\right] + \frac{\tau}{25}, \tag{3c}$$

$$v_{x,D}(y, \tau; \delta) = [1 + \delta\sin(\pi y/36)]\left[1 - \frac{\tau}{25}\right] + \frac{\tau}{25}, \tag{3d}$$

for $0 \leqslant \tau \leqslant 25$, has the same uniform profile [$v_{x,in}(y, \tau) = 1$] for $\tau \geqslant 25$, where x_{in} is the location of the upstream computational inlet, discussed in Sec. II C. These transients (Figs. S1(a)–S1(d) [29]) vary on a timescale (25 convective time units) orders of magnitude larger than the time-step size, and also considerably larger than the timescale for vortex shedding and cylinder motion. [The fifth transient, denoted by E, is uniform flow for $\tau \geqslant 0$, i.e., $v_{x,E}(y, \tau) = 1$.] In Eqs. (3a)–(3d), α, β, γ, and δ characterize the degree of asymmetry of the prescribed inlet transient, with large values corresponding to strong asymmetry, and each of the limits $\alpha \to 0$, $\beta \to 0$, $\gamma \to 0$, and $\delta \to 0$ corresponding to uniform flow for all $\tau \geqslant 0$. Unless otherwise specified, $\alpha = \beta = \gamma = \delta = 1$.

In each case, the initial condition in our domain is a divergence-free velocity field $\mathbf{v}(x, y, 0) = \mathbf{e}_x v_{x,in}(y, 0)$ with a cross-stream profile identical to the initial inlet velocity. The compatibility of the initial and inlet profiles at $\tau = 0$ and $x = x_{in}$ is important in that it avoids incompatibilities between a specified nonuniform inlet condition and a uniform initial condition in the domain, or between a uniform inlet condition and a nonuniform initial condition. Also, in each case, the initial position of the NES mass is $\theta_i = \pi/2$ unless otherwise indicated, and the initial velocity of the NES mass is zero. The cylinder is initially motionless at its equilibrium position.

In searching for coexisting long-time solutions, use of multiple inlet transients over $0 \leqslant \tau \leqslant 25$ is equivalent to use of multiple initial conditions at $\tau = 25$. The instantaneous velocity and

pressure fields at $\tau = 25$, as well as the rectilinear displacement and velocity of the cylinder and angular position and velocity of the rotating mass at $\tau = 25$, are determined by the initial-value problem (beginning at $\tau = 0$) with the imposed inlet transient. There is thus a mapping from each combination of an inlet transient over $0 \leqslant \tau \leqslant 25$ and an initial condition at $\tau = 0$, to an initial condition at $\tau = 25$, with the mapping being effected by the governing equations.

C. Computational approach

Solutions are approximated computationally using the open-source, spectral-element Navier-Stokes solver Nek5000 [30], whose adaptation to the problem at hand is described by Tumkur *et al.* [23]. The computational domain extends 72 cylinder diameters in the cross-stream direction and $96D$ in the streamwise direction, with the undisplaced cylinder center located $24D$ away from the inlet boundary and equidistantly from the side walls. Our production runs use a mesh with 2784 spectral elements, polynomial degree $N = 5$, and time-step size $\Delta \tau = 2 \times 10^{-3}$. For these values of the parameters, the long-time solutions are qualitatively similar to those where we simultaneously halved the time-step size, quadrupled the number of elements, and increased the polynomial degree to nine (Figs. S2(a)–S2(h) [29]).

As in the work of Tumkur *et al.* [23], the time-step size used is sufficiently small that no fluid-structure interaction iteration is required.

III. PHASE DIAGRAM AND STABILITY BOUNDARY

When an SSMC is found, we define the final angular position of the NES mass by

$$\theta_\infty = \lim_{\tau \to \infty} \theta(\tau). \tag{4a}$$

In this case, the *flow* is symmetric about $y = 0$, even though the position of the NES mass might not be. All other long-time solutions we found are unsteady, with the flow being asymmetric at each time.

In what follows, $m^* = 10$, $\varepsilon_p = 0.3$, $\zeta = 4/3$, and $\bar{r}_0 = 0.3$ unless otherwise stated.

A. Overview of the phase diagram

For the stated combination of density ratio (m^*), NES parameters (ε_p, ζ, and $\bar{r}_0$), and initial angular position $\theta_i = \pi/2$, the solid and dotted lines in Fig. 2 show linear stability boundaries for the NES-less and NES-equipped cases, respectively, as determined by Tumkur *et al.* [23] using inlet transient A with $\alpha = 10^{-4}$. The 279 tilted squares, pentagons, upright squares, and circles correspond to cases in which inlet transients A–E with $\alpha = 1$ lead to four, three, two, and one long-time solutions, respectively. (No more than one SSMC solution is counted in making this assignment, regardless of the number of values of θ_∞ found with different inlet transients.) Moreover, for each symbol shape (and hence for each number of distinct long-time solutions), there is a one-to-one correspondence between the symbol color and the combination of long-time solutions found.

For each combination of g_n^* and Re in Fig. 2, the number and type of SSMC solutions is indicated using one or more internal lines. A horizontal line denotes a case in which the symmetric inlet transient does not lead to cylinder motion, so that the rotating mass is never displaced. A vertical line denotes a case in which at least one inlet transient gives rise to an SSMC solution with $|\theta_\infty - n\pi| \leqslant 10^{-6}\pi$ (n being an integer). A diagonal cross denotes a case where at least one inlet transient gives rise to an SSMC solution with $|\theta_\infty - n\pi/2| \geqslant 10^{-6}\pi$ for all integers n. For symbols containing more than one of these lines, the interpretation is "additive." Thus, an open circle with vertical and horizontal lines and a diagonal cross correspond to the case in which every inlet transient leads to an SSMC solution, with at least one being $\theta_\infty = \pi/2$, at least one being $\theta_\infty = n\pi$, and at least one being $\theta_\infty \neq m\pi/2$, where m and n are integers. Similarly, a pentagon with a horizontal line
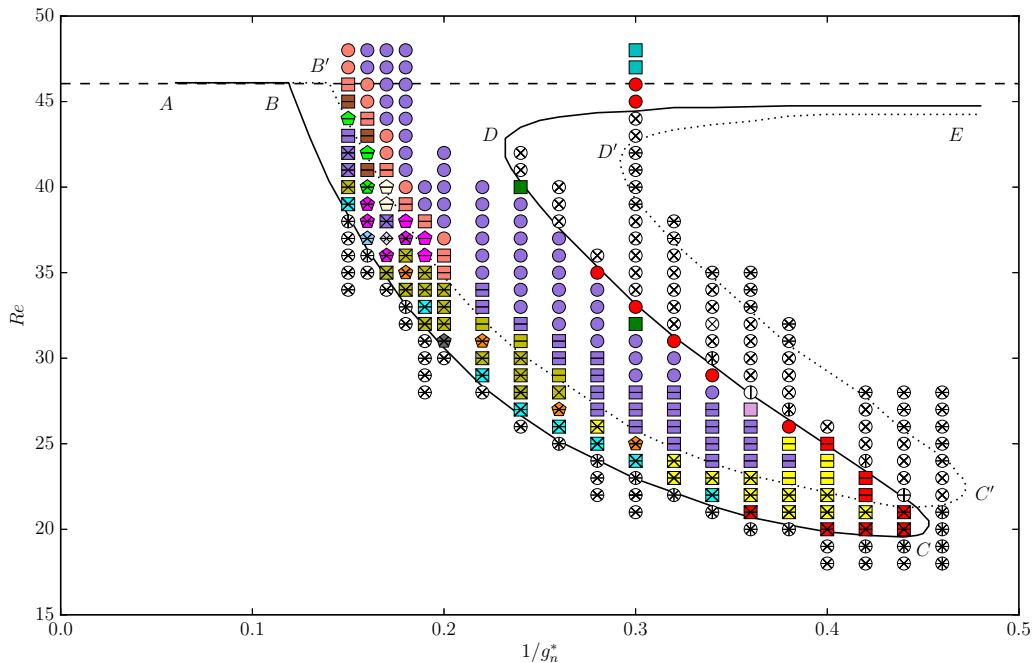
FIG. 2. Phase diagram. Standard VIV (SVIV) solutions, ● ■; fully developed chaotic (FDC) solutions, ● ■; slowly decaying cycle (SDC) solutions, ● ■; steplike chaotic (SLC) solutions, ■; quasiperiodic (QP) solutions, ■; back-and-forth periodically rotating (BAFPR) solutions, ■; periodic, predominantly unidirectionally rotating (PPUR) solutions, ■; SVIV + SLC, ■; SVIV + BAFPR, ■; SVIV + FDC, ■; BAFPR + SLC, ⬠; QP + SLC, ⬠; QP + PPUR, ⬠; FDC + PPUR, ⬠; SLC + PPUR, ⬠; SDC + PPUR, ⬠; and SLC + PPUR + BAFPR, ◇. The dashed horizontal line, solid line, and dotted line denote the stability boundary for the fixed cylinder, NES-less sprung cylinder, and NES-equipped sprung cylinder with $\varepsilon_p \sin^2 \theta_s = 0.3$, respectively.

corresponds to a case in which the only SSMC solution found has $\theta_\infty = \pi/2$, and two unsteady long-time solutions also exist. Situations in which all of the inlet transients give rise to unsteady long-time solutions are denoted by symbols with no internal lines.

As a consequence of the mapping from an inlet transient and $\tau = 0$ initial condition to a $\tau = 25$ "initial condition," the existence of more than one long-time attracting solution for a given set of parameters demonstrates that the initial condition space for this autonomous system can be decomposed into parts, from each of which attraction occurs to a different long-time solution. While it is typically not trivial to identify basins of attraction in the initial condition space even for a finite-dimensional system in which the basins are neither fractal nor riddled [31–35], the difficulty of doing so in the infinite-dimensional initial condition space for *any* nonlinear partial differential equation is daunting. One can in principle project the function space of initial conditions onto a finite-dimensional space and divide that into basins of attraction. But as far as we know, there has been only one attempt to identify basins of attraction in a flow, namely the work of Skufca *et al.* [36], who considered a nine-dimensional reduced-order (ODE) model of a parallel shear flow, and delineated basins of attraction in a two-dimensional projection of the nine-dimensional initial condition space.

We do not attempt to fully explore the initial condition space (or the space of inlet transients) and thus make no claim for completeness of our "collection" of long-time solutions for any combination of Re and g_n^*. We consider only integer Re, for which we focus on identifying qualitatively different long-time solutions. We make no claim regarding solutions at fractional Re values and

do not characterize routes to chaos, transitions as Re or g_n^* varies, or basins of attraction in the infinite-dimensional space of initial conditions or in any projection thereof.

B. Relationship to the stability boundary

As discussed by Tumkur *et al.* [23], the two stability boundaries shown in Fig. 2 pertain to an SSMC base flow and were computed using noninfinitesimal disturbances with small asymmetry, along the lines of Zielinska and Wesfreid [37]. For the NES-less case, the stability boundary ABCDE separates conditions under which sufficiently small disturbances to the base flow decay for combinations of Re and g_n^* on one side and do not decay on the other side. For the NES-equipped case, we specify an initial value $\theta_i = \pi/2$ and note that the stability boundary AB′C′D′E separates situations where asymmetric disturbances decay from those in which they do not. (As discussed below, the symmetric inlet transient E can lead to instability only as a result of asymmetries in the numerics.) We also note that the steady symmetric flow with $\theta_i = \pi/2$ can evolve to an SSMC solution in which the angular position of the NES mass has a different value. If that outcome occurred when *infinitesimal* disturbances were used, then there would be two possibilities, in which the final position θ_∞ of the NES mass differs infinitesimally or noninfinitesimally from $\pi/2$. In terms of a base state corresponding to an SSMC solution and $\theta_i = \pi/2$, we characterize the first situation as stable, and the second as unstable because the disturbance grew to a noninfinitesimal amplitude before ultimately decaying to $\theta_\infty \neq \theta_i$. Because the stability boundaries were determined using noninfinitesimal disturbances, a final value $\theta_\infty = \pi/2$ is expected to arise in only two cases: (a) when the disturbance is symmetric and the NES mass is not displaced and (b) as a limiting case when the asymmetry of the inlet transient tends to zero. As discussed by Tumkur *et al.* [23], both possibilities have been realized.

Figure 2 shows that in the portion of the Re-$1/g_n^*$ plane in which the NES-less case is linearly stable, only SSMC solutions are found. Moreover, in the portion of the Re-$1/g_n^*$ plane in which the NES-less case is linearly stable *and* the NES-equipped case is unstable, none of the SSMC solutions found has $\theta_\infty = \pi/2$. This includes those for symmetric inlet transient E, showing that in this part of the Re-$1/g_n^*$ plane, the initial SSMC solution is destabilized by small asymmetries in the numerics. In the portion of the Re-$1/g_n^*$ plane in which the NES-equipped case is linearly stable and the NES-less case is unstable, additional computations for inlet transients with smaller asymmetries ($\alpha = \beta = \gamma = \delta = 10^{-1}, 10^{-2}, 10^{-3}$, and 10^{-4}) give results consistent with the linear stability boundary (Table S1 [29]). The dependence of the final state on disturbance amplitude (shown for inlet transient A in Table S1 [29]) shows that the SSMC solution with $\theta_i = \pi/2$ is subject to finite-amplitude instability in this portion of the Re-$1/g_n^*$ plane.

As discussed by Tumkur *et al.* [23], the stability boundaries are triple-valued over a range of g_n^*, and linear stability of an SSMC solution depends on Re, g_n^*, m^*, ζ, and $\varepsilon_p \sin^2 \theta_s$, but not on $\bar{r}_0$, or separately on either ε_p or θ_s (where θ_s is the steady NES angular position). Based on this or examination of Eqs. (2a) and (2b), it is clear that linear stability analysis of the SSMC solution with $\theta_s = n\pi$ reduces to the NES-less case. (On physical grounds, this must be so because there is no inertial coupling if $\theta = n\pi$ and $d\theta/d\tau = 0$.) As discussed in Sec. IV, for each combination of Re, g_n^*, m^*, and ζ for which an SSMC solution with $\theta_s = \pi/2$ is linearly stable, there is a range of stable values of $\varepsilon_p \sin^2 \theta_s$, and so stable SSMC solutions do not have a unique θ_s, except when $\theta_s = n\pi$ is the only stable SSMC solution.

IV. NATURE OF THE DISTINCT SOLUTIONS

Here, we categorize and discuss the computed solutions over a range of Re and $1/g_n^*$, largely based on the long-time dynamical behavior of the rotating mass, which is qualitatively distinct for each unsteady long-time solution, and of the wake. This focus is appropriate because, as discussed in Sec. II C, the long-time behavior is qualitatively insensitive to the details of the numerical discretization, provided that the discretization provides sufficient temporal and spatial resolution.

The relationship between the temporal complexity of the NES mass rotation, cylinder displacement, and flow is of interest from the standpoint of using one or two of them as diagnostics for the remainder. There are two distinct cases. First, when the NES mass does not rotate, if either the cylinder displacement or the flow is steady, time-periodic, quasiperiodic, or chaotic, then so is the other, on account of the coupling through Eq. (2a) and the boundary conditions at the fluid/cylinder interface. In the second case, when the NES mass rotates, Eqs. (2a) and (2b) show that neither the flow nor y_1 can be steady and that if any one of the NES mass rotation, cylinder motion, or flow is periodic, quasiperiodic, or chaotic, then so are the others. Note that Eq. (2b), considered in isolation as a second-order ODE for θ with $y_1(\tau)$ being a given periodic function, allows for the possibility of a time-periodic cylinder motion giving rise to chaotic NES mass rotation. But when Eq. (2a) is also considered, it becomes clear that a periodic y_1 is incompatible with a chaotic θ.

The transient behavior of the asymptotically periodic and quasiperiodic solutions (all of which include a chaotic transient [38]), and the long-time chaotic solutions, is sensitive not only to initial conditions but also to the details of the numerical discretization. When the discretization provides sufficient spatial and temporal resolution, this sensitivity has very little effect on the statistics (broadly defined) of the long-time solution. Sensitivity of transient or long-time chaotic behavior to discretization likely corresponds to sensitivity to initial conditions in a physical experiment. For such solutions, the reported behavior is thought to be representative, in the same sense that, for a broad class of physical systems, chaotic behavior in a single realization of a physical experiment is thought to be representative of what would be observed in a larger ensemble. Evidence for this hypothesis can be found in the results presented in Sec. IV D.

A. Steady solutions

For an SSMC solution with any value of θ_s, the flow is identical to that past a fixed cylinder. As noted in Sec. III B, for an NES-equipped cylinder the linear stability of an SSMC solution depends on only Re, g_n^*, m^*, ζ, and $\varepsilon_p \sin^2 \theta_s$. For Re $= 36$, $1/g_n^* = 0.17$, and inlet transient A with $\alpha = 10^{-4}$ (used to compute the stability boundaries), Table I shows that for $\varepsilon_p = 0.3$ and 0.6, there is a limited range of angular positions of the NES mass for which the SSMC solution is stable. That range has upper and lower bounds $\pi/2$ and $\theta_{\text{crit}} = \arcsin(\Gamma/\varepsilon_p)^{1/2}$, respectively, where $\Gamma \approx 0.0912$ is the minimum value of the "combination" parameter $\varepsilon_p \sin^2 \theta_s$ for which stability is possible. For $\theta_i = 0$, a standard VIV solution is the long-time solution. Different long-time solutions are found for larger values of $\varepsilon_p \sin^2 \theta_i$ in the range $0 < \varepsilon_p \sin^2 \theta_i < 0.0912$, where any SSMC solution necessarily has $\theta_\infty \neq \theta_i$, with $\arcsin(\Gamma/\varepsilon_p)^{1/2} \leqslant \theta_\infty \leqslant \pi/2$.

The physical mechanism is as follows. For $\theta_s = 0$, the NES has no consequence for linear stability and the only possible long-time solutions are the standard VIV solution corresponding to an NES-less sprung cylinder, and an SSMC solution. On the other hand, the more θ_s differs from an integer multiple of π, the more potential there is for the NES mass to respond to rectilinear cylinder motion arising from asymmetric disturbances. This response can bleed off kinetic energy associated with that rectilinear motion, damping disturbances. When θ_s is close to an integer multiple of π, the NES mass has little "leverage" to bleed energy from the rectilinear motion, and some disturbances which would have decayed for larger θ_s can now grow.

B. Time-periodic solutions

1. Standard VIV solutions

For standard VIV, the NES has no dynamical effect, and the two-dimensional flow and cylinder motion are time periodic (in this range of Re) and identical to the NES-less case. Conversely, if θ is always equal to an integer multiple of π, cylinder oscillation corresponds to standard VIV, and Eqs. (2a) and (2b) show that the rectilinear motion of the cylinder is coupled only to the flow. Consistent with what is known about standard VIV [3], we believe that when this solution is linearly stable for $m^* \leqslant 10$, there are no additional unsteady long-time solutions with θ_∞ equal to an integer

TABLE I. Relationship between values of the combined parameter $\varepsilon_p \sin^2 \theta_i$ and long-time solutions using inlet transient A with $\alpha = 10^{-4}$, at Re $= 36$ and $1/g_n^* = 0.17$, computed for $\varepsilon_p = 0.3$ and 0.6 (SVIV, standard VIV solution; SSMC†, steady, symmetric, motionless-cylinder solution with $\theta_\infty = \theta_i$; SSMC*, steady, symmetric, motionless-cylinder solution with $\theta_\infty \neq \theta_i$; SLC, steplike chaotic solution; PPUR, periodic, predominantly unidirectionally rotating solution; QP: quasiperiodic solution).

| | $\varepsilon_p = 0.3$ | |
θ_i/π	$\varepsilon_p \sin^2 \theta_i$	Long-time solution
0.0000	0.0000	SVIV
0.0100	0.0003	PPUR
0.0500	0.0073	SLC
0.1000	0.0286	SLC
0.1200	0.0407	SLC
0.1300	0.0473	SLC
0.1350	0.0508	SLC
0.1400	0.0544	PPUR
0.1450	0.0581	SLC
0.1500	0.0618	SLC
0.1540	0.0649	SLC
0.1580	0.0680	SLC
0.1620	0.0712	SLC
0.1660	0.0745	SSMC*
0.1859	0.0912	SLC
0.1860	0.0913	SSMC†
0.1880	0.0930	SSMC†
0.1900	0.0948	SSMC†
0.1920	0.0965	SSMC†
0.1960	0.1001	SSMC†
0.1980	0.1019	SSMC†
0.2000	0.1036	SSMC†
0.3000	0.1964	SSMC†
0.4000	0.2714	SSMC†
0.4500	0.2927	SSMC†
0.4900	0.2997	SSMC†
0.5000	0.3000	SSMC†
	$\varepsilon_p = 0.6$	
θ_i/π	$\varepsilon_p \sin^2 \theta_i$	Long-time solution
0.0000	0.0000	SVIV
0.0100	0.0006	SSMC*
0.0500	0.0147	QP
0.1000	0.0573	QP
0.1275	0.0912	QP
0.1276	0.0913	SSMC†
0.1300	0.0946	SSMC†
0.1500	0.1237	SSMC†
0.2000	0.2073	SSMC†
0.3000	0.3927	SSMC†
0.4000	0.5427	SSMC†
0.5000	0.6000	SSMC†
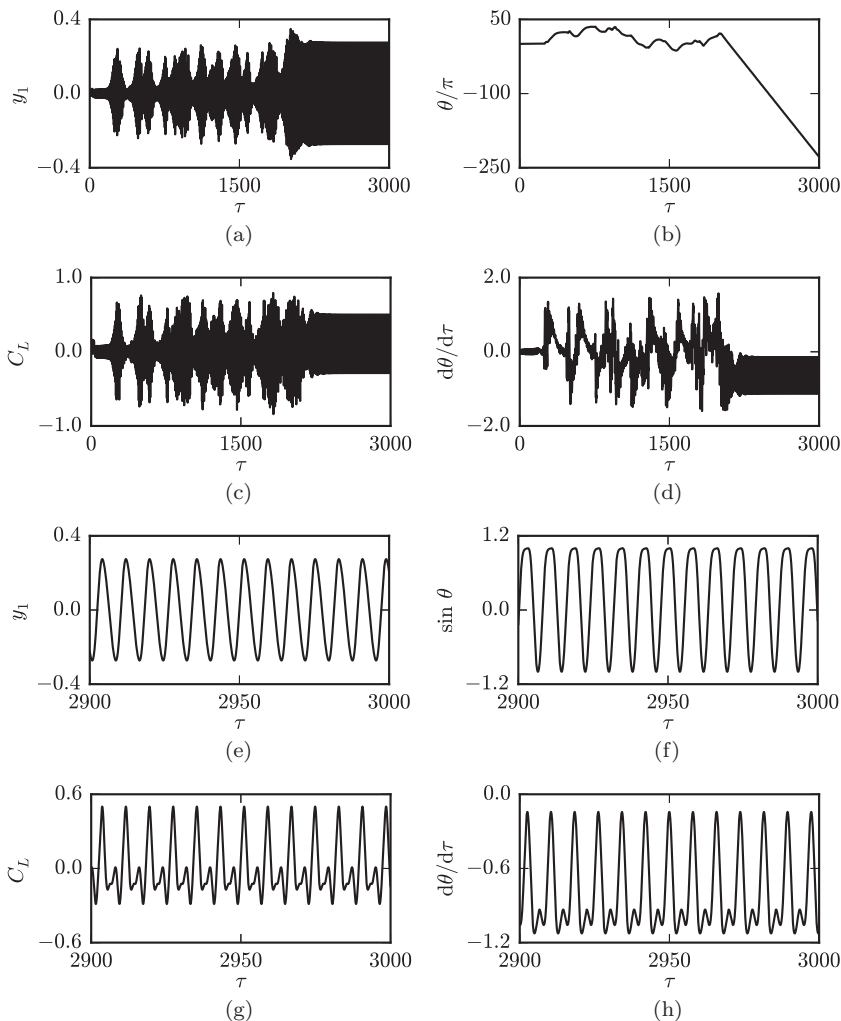
FIG. 3. Time series for the PPUR solution found with inlet transient C at Re = 38 and $1/g_n^* = 0.18$: (a) cylinder displacement, (b) NES angular position, (c) lift coefficient, (d) NES angular velocity, and [(e)–(h)] details of long-time behavior of quantities shown in panels (a)–(d).

multiple of π. For Re = 35 and $1/g_n^* = 0.28$ (leftmost red circle in Fig. 2) and inlet transient A, coupling NES mass rotation to the cylinder's rectilinear motion leads to growth of disturbances in y_1 and θ during an interval of transient chaos (see Movie 1 in the Supplemental Material [29]), followed by an asymptotic approach to standard VIV with $\theta_\infty = 0$ (see Figs. S3(a)–S3(h) [29]). Asymptotic values of θ equal to even and odd multiples of π have been observed, depending on the transient chaotic behavior, which in turn depends on the specified inlet transient and the detailed error properties of the computational algorithm.

2. Periodic, predominantly unidirectionally rotating (PPUR) solutions

Figures 3(a)–3(h) show time series for Re = 38 and $1/g_n^* = 0.18$, using inlet transient C. A notable feature is the very long chaotic transient (extending over 2000 convective time units) before the trajectory settles down to a time-periodic solution that could have been overlooked had the simulation been terminated earlier. The chaotic transient features several episodes ($340 < \tau < 400$,
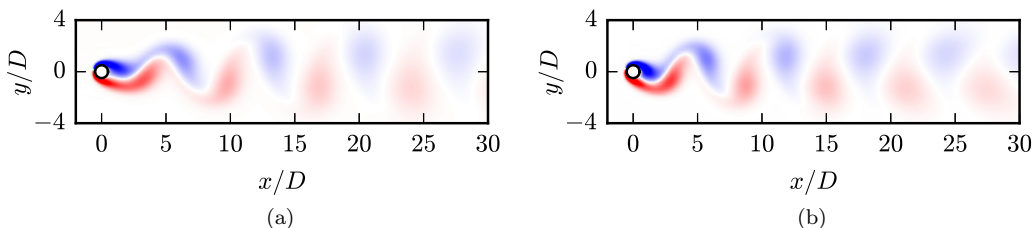
FIG. 4. Spanwise vorticity for (a) the PPUR solution found with inlet transient C at Re = 38 and $1/g_n^* = 0.18$, at $\tau = 2878.8$, and (b) NES-less VIV for the same parameters and the same phase of cylinder motion as in panel (a).

$660 < \tau < 700$, and briefly near $\tau = 1020$, 1180, 1350, 1530, and 1630; see Movie 2 in the Supplemental Material [29]) of significant wake elongation and symmetrization. Elongation and symmetrization are not found (here or in previous work) in the NES-less case, showing that the NES is necessary for these flow phenomena. In the asymptotic state [Figs. 3(e)–3(h)], the NES mass rotates exclusively in the counterclockwise direction, swinging through a full 2π during each period. (For an inlet transient with opposite symmetry, it is easy to prove that the NES mass rotates in the opposite direction.) Comparison of the asymptotic limit cycle [Fig. 4(a)] to the NES-less standard VIV case [Fig. 4(b)] shows that the wakes are similar.

That the solution continues to wander through the phase space before finally being attracted to a time-periodic solution at around $\tau = 2100$ suggests that both the standard VIV solution (to which the trajectory was not attracted after the inlet transient) and SSMC solution are nonattracting sets in the phase space, whose existence is a necessary condition for transient chaos [38].

If the first factor in the first term on the right-hand side of inlet transient C is modified to $1 + y/36.001$, then the pre-PPUR transient (see Figs. S4(a)–S4(d) [29]) is quite different than for the unmodified inlet transient C [Figs. 3(a)–3(d)], with the duration of transient chaos being significantly shorter. This sensitivity to inlet transient details is reminiscent of sensitivity to initial conditions in systems displaying transient chaotic behavior [38] and follows directly from the relationship between inlet transients and initial conditions discussed in Sec. II B.

For Re = 36 and $1/g_n^* = 0.17$ (the parameters for which SSMC solutions were presented above) with inlet transient A, Movie 3 [29] and Figs. 5(a)–5(h) show that the solution settles into a PPUR state by about $\tau = 200$. The NES mass rotates predominantly counterclockwise, but with some reversal during a small fraction of each cycle [Fig. 5(h)]. Power spectral analysis shows that y_1 has a dominant dimensionless frequency of 0.139, with a relatively weak harmonic contribution at $fD/U = 0.278$. The lift and drag coefficients show significant response at both frequencies. In contrast to the PPUR solution discussed above for Re = 38 and $1/g_n^* = 0.18$, the PPUR solution for Re = 36 and $1/g_n^* = 0.17$ (both with inlet transient A) involves a definite "hesitation" in the angular position of the NES mass (near $\theta = 3\pi/2$) during each cycle, with the NES mass coming to rest and quickly executing a small clockwise reversal, before resuming its counterclockwise motion. Vortex shedding is strong from the start, with no discernible partial stabilization or vortex elongation.

3. Back-and-forth periodically rotating (BAFPR) solutions

For Re = 24, $1/g_n^* = 0.4$, and inlet transient A, Figs. 6(a)–6(h) and Movie 4 [29] show that during an initial transient ($0 < \tau < 35$), relatively rapid, large-amplitude cylinder motion significantly disturbs the early-time spanwise vorticity distribution, which is convected downstream and out of the computational domain. During this time, the cylinder and NES mass undergo large rectilinear and angular displacements, respectively. This is followed by an interval (from about $\tau = 50$ to about $\tau = 150$) that begins with considerable vortex elongation (see Movie 4 in the Supplemental Material [29]) and small-amplitude cylinder motion and NES mass rotation about $\theta = 0$. As time progresses, oscillations in y_1 and C_L continue to grow, the NES mass remains nearly
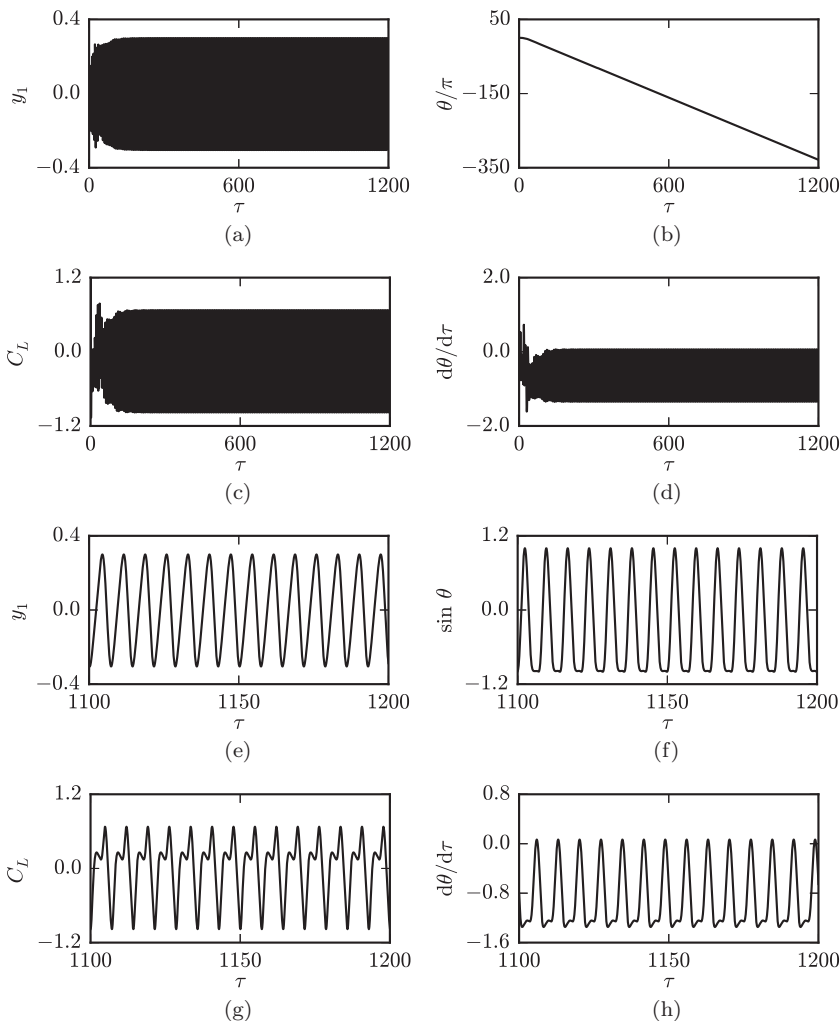
FIG. 5. Time series for the PPUR solution (with reversal) found with inlet transient A at Re $= 36$ and $1/g_n^* = 0.17$: (a) cylinder displacement, (b) NES angular position, (c) lift coefficient, (d) NES angular velocity, and [(e)–(h)] details of long-time behavior of quantities shown in panels (a)–(d).

stationary near $\theta = 0$, and the solution seemingly approaches standard VIV. At about $\tau = 480$, however, the amplitude of oscillation of the NES mass grows rapidly. As shown in Fig. 6(c), this begins with "split-peak oscillations," leading to large "spikes" in the lift, and ultimately to a time-periodic solution in which split-peak oscillations of the NES mass persist [Fig. 6(h)]. The increasing deviation of the NES-equipped case from the NES-less case beginning near $\tau = 480$ is associated with the NES mass rotation becoming more closely coupled to the cylinder motion, and hence to the flow, as θ increases. The wake is qualitatively similar to what is seen for standard VIV [compare Fig. 7(a) to Fig. 7(b)]. At long times, y_1, C_L, and θ are periodic (Figs. S5(a)–S5(c) [29]), with a slightly richer harmonic content in the Fourier spectrum for C_L than for y_1 and θ. The dominant frequencies for C_L, y_1, and θ are close to St, St, and St/2 (where St is the Strouhal frequency), respectively, strongly suggesting a mechanism of 1:1:2 internal resonance among the lift, rectilinear cylinder motion, and rotation of the NES mass, respectively.
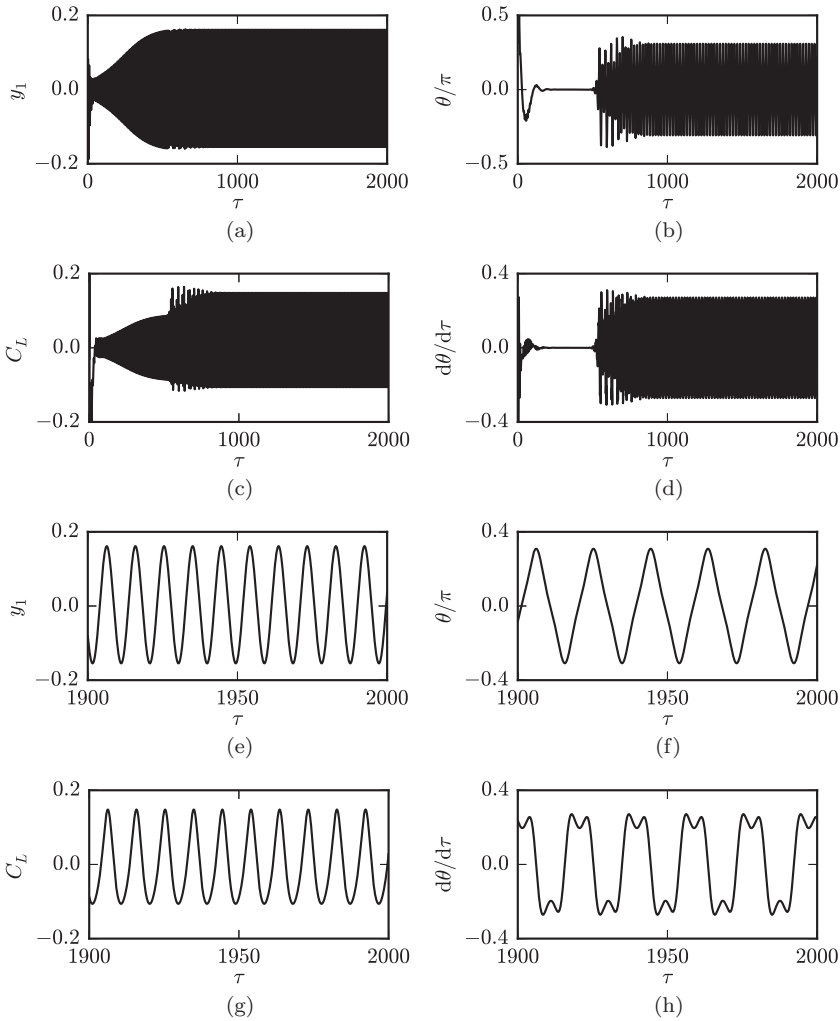
FIG. 6. Time series for the BAFPR solution found with inlet transient A at Re $= 24$ and $1/g_n^* = 0.4$: (a) cylinder displacement, (b) NES angular position, (c) lift coefficient, (d) NES angular velocity, and [(e–h)] details of long-time behavior of quantities shown in panels (a)–(d).
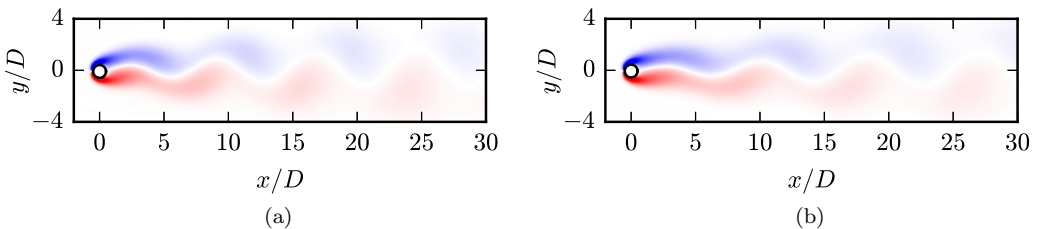

FIG. 7. Spanwise vorticity for (a) the BAFPR solution found with inlet transient A at Re $= 24$ and $1/g_n^* = 0.4$, at $\tau = 1804$, and (b) NES-less VIV for the same parameters and the same phase of cylinder motion as in panel (a).
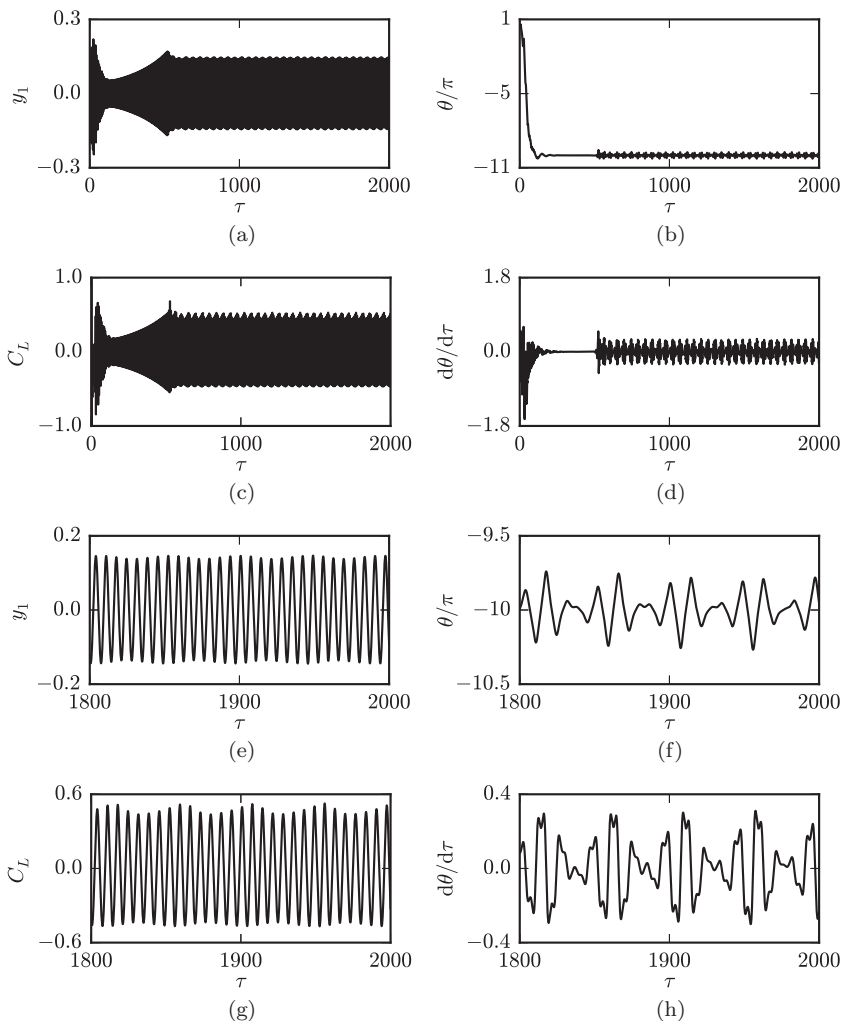
FIG. 8. Time series for the QP solution found with inlet transient A at Re = 33 and $1/g_n^* = 0.19$: (a) cylinder displacement, (b) NES angular position, (c) lift coefficient, (d) NES angular velocity, and [(e)–(h)] details of long-time behavior of quantities shown in panels (a)–(d).

C. Quasiperiodic solutions

For Re = 33 and $1/g_n^* = 0.19$, Figs. 8(a)–8(h) and Movie 5 [29] show that inlet transient A gives rise to a long transient in which the amplitude of oscillations in y_1 decays from greater than 0.2 to about 0.05, and the NES mass rotates counterclockwise, approaching -10π. As the NES mass becomes nearly motionless near -10π, a wake instability sets in, and the oscillation amplitudes of y_1 and C_L linearly grow, leading to increased wake asymmetry and unsteadiness. By about $\tau = 520$, the amplitude of y_1 has increased to the point where rotation of the NES mass is excited, and the system rapidly approaches a long-time solution that appears to be quasiperiodic, and in which the wake is quite different from that for an NES-less linearly sprung cylinder [compare Figs. 9(a) and 9(b)].

Figures 10(a) and 10(c) and Tables S2(a) and S2(c) [29] show that the dominant frequency for y_1 and C_L is $f_1 = 0.1449$, close to the natural frequency [$1/(0.19 \times 33) = 0.1594$] of the linearly sprung cylinder. For θ, Fig. 10(b) shows that the dominant frequency is $f_2 = 0.0834$. For y_1
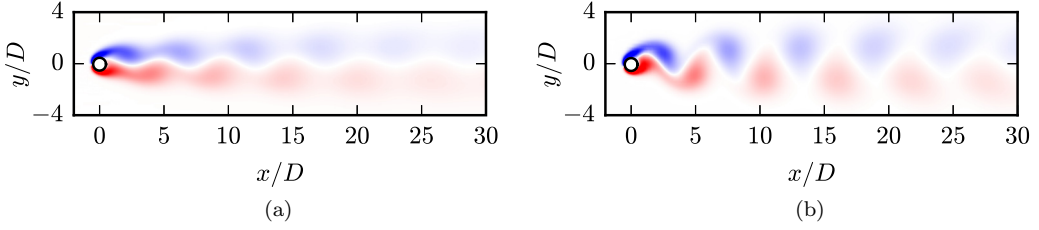
FIG. 9. Spanwise vorticity for (a) the QP solution found with inlet transient A at $Re = 33$ and $1/g_n^* = 0.19$, at $\tau = 1950.8$, and (b) NES-less VIV for the same parameters and the same phase of cylinder motion as in panel (a).

(using the 18 frequencies having the highest energy), θ (16 frequencies), and C_L (15 frequencies), respectively, each frequency can be written as a sum of rational multiples of the essentially incommensurable frequencies f_1 and f_2, whose ratio is 0.576 (Tables S2(a)–S2(c) [29]). (The closest ratio of "small" integers is $5/7 = 0.571428...$. The closest ratio of integers with denominator less than 26 is $11/19 = 0.578947...$.) The rational numbers in the "a" and "b" columns of Tables S2(a)–S2(c) [29] are multiples of $1/3$. For the long-time solution, the wave forms for y_1 [Fig. 8(e)] and C_L [Fig. 8(g)] are quite similar. The power spectrum for y_1 [Fig. 10(a)] shows a (small) peak near 0.0205, corresponding to the modulation frequency, which is the difference between four pairs of frequencies in each of the three power spectra (see Tables S2(a)–S2(c) [29]).

In the asymptotic regime, $dy_1/d\tau$ fluctuates about a mean of essentially zero. The long-time θ and $d\theta/d\tau$ [Figs. 8(f) and 8(h), respectively] are strongly modulated, at a frequency of 0.019, with no significant power at the frequency dominant for y_1 and C_L. The angular motion has its two most energetic peaks at 0.0834 and 0.1039, separated by $0.0205 = (0.1449 - 0.0834)/3$, the modulation frequency for y_1, C_L, and θ.

Although the dominant frequencies (0.1449 and 0.0834) of y_1 and θ "cross over" into each other's time series (each extracted frequency in y_1 and θ can be written as a rational linear combination of the two dominant frequencies; see Tables S2(a)–S2(c) in the Supplemental Material [29]), the modulation frequencies (0.0205 for y_1 and 0.019 for θ) are not among the most energetic frequencies extracted.

Finally, modulation of C_L is somewhat asymmetric [Fig. 8(g)], being smaller near the minima than at the maxima. Modulation of y_1 is considerably less asymmetric.
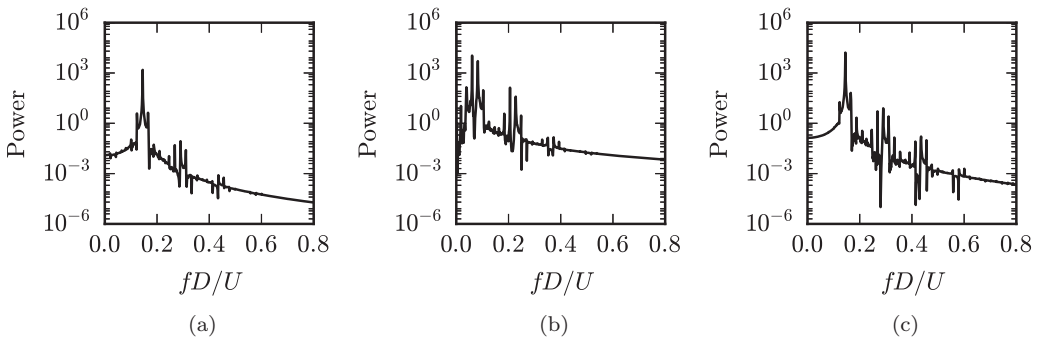

FIG. 10. Fourier spectra of (a) y_1, (b) θ, and (c) C_L computed over the time window $1200 \leqslant \tau \leqslant 2000$ for the QP solution found with inlet transient A at $Re = 33$ and $1/g_n^* = 0.19$.

D. Temporally chaotic solutions

1. Fully developed chaotic (FDC) solutions

For Re = 31, $1/g_n^* = 0.28$, and inlet transient C, Figs. 11(a)–11(e) and Movie 6 [29] show that after an initial transient (from $\tau = 0$ to about $\tau = 70$), the trajectory settles into a chaotic state, whose nature is evident from the broadband frequency content of the wavelet spectra for y_1, $\sin\theta$, and C_L (Figs. S6(a)–S6(c) [29]). By comparison to the standard VIV case [Fig. 12(d)], Figs. 12(a) and 12(b) show that the wake structure is considerably affected by the NES, not only in the near field, with recurring episodes featuring noticeable elongation of the attached vorticity [Fig. 12(a)], but also in the far field, with less organized vortex structures [Fig. 12(b)]. Figure 12(c) shows that during other time intervals, the wake structure is reminiscent of standard VIV [Fig. 12(d)].

Movie 6 [29] shows that in the asymptotic regime, the cylinder displacement shows a number of peaks (e.g., near $\tau = 1170$, 1248, 1308, 1386, and 1472), recurring at roughly equal intervals, interlaced with very short intervals of small cylinder displacement. During each of the latter relatively quiescent episodes, the wake undergoes considerable elongation and significant symmetrization, corresponding to minima in the time series of drag [Fig. 11(e)]. But just as an SSMC solution can give rise (via instability) to the Kármán vortex street in the NES-less case, we believe that the partially symmetrized flow found here elongates until it becomes unstable with respect to a wake instability. Judging from Movie 6 [29], the streamwise extent of wake elongation appears to be roughly the same in each episode.

To characterize the chaotic response, we consider the streamwise and cross-stream velocity components at a point fixed with respect to an inertial reference frame and located in the near wake, $1.25D$ downstream of the cylinder center and $1D$ above the midline $y = 0$ (referred to as point P), along with their wavelet and Fourier spectra (Figs. S7(a)–S7(f) [29]). As with y_1, θ, and C_L, the broadband frequency content of the wavelet and Fourier spectra for the two velocity components evidences the chaotic nature of the flow. Qualitatively identical results are obtained for the two velocity components at a point $3.25D$ downstream of the undisplaced cylinder center and $1D$ above the midline. (We refer to this as point Q.)

Figures 13(a)–13(f) show the normalized autocorrelation of $v_{x,P} \equiv v_x(x_P, y_P, \tau)$, the normalized cross correlations of $v_{x,P}$, $v_{y,P} \equiv v_y(x_P, y_P, \tau)$ and $dy_1/d\tau$ with each other, the normalized cross correlation of $v_{x,P}$ and $v_{x,Q} \equiv v_x(x_Q, y_Q, \tau)$, and the normalized cross correlation of $dy_1/d\tau$ with C_L, where we define the normalized cross correlation of $q(\tau)$ and $s(\tau)$ as

$$a_{q,s}(\tau_c) = \frac{\int_{\tau_1}^{\tau_2} q'(\tau)s'(\tau + \tau_c)\,d\tau}{(\tau_2 - \tau_1)[\langle q'^2\rangle\langle s'^2\rangle]^{1/2}}, \tag{5}$$

where $q'(\tau) = q(\tau) - \langle q\rangle$, $s'(\tau) = s(\tau) - \langle s\rangle$, and the angle brackets denote mean quantities. For the normalized autocorrelation, we simply replace $s(\tau)$ by $q(\tau)$. The most striking feature of these plots is that none decays as the lag τ_c increases to 1200 convective time units, corresponding to almost 200 shedding cycles. This is in stark contrast to the results shown in Figs. 20(g) and 20(h) of Tumkur *et al.* [23], where the cross correlations of the cylinder velocity with the two velocity components at point P showed significant decay over lag times much shorter than observed in Figs. 13(a)–13(f). The difference between our nondecaying (or very slowly decaying) correlations and those of Tumkur *et al.* [23] is largely due to the relatively "weakly chaotic" nature of the present time series for $v_{x,P}$, $v_{y,P}$, $v_{x,Q}$, and $dy_1/d\tau$, as revealed by comparison of the wavelet spectra in Figs. S7(c) and S7(d) [29] to those in Figs. 20(c) and 20(d) of Tumkur *et al.* [23] and of the power spectra in Figs. S7(e) and S7(f) [29] to those in Figs. 20(e) and 20(f) of Tumkur *et al.* [23]. It is clear that the response in the present case, while definitely broadband, is more strongly dominated by two frequencies than is the case for the higher Re system considered by Tumkur *et al.* [23]. The autocorrelation of $v_{x,P}$, the cross correlations of $v_{x,P}$ with either $v_{x,Q}$, $v_{y,P}$, or $dy_1/d\tau$, and the cross correlation of $v_{y,P}$ with $dy_1/d\tau$ are essentially identical, largely because the velocity components at points P and Q, and the cylinder velocity, are strongly correlated. The cross correlation of $dy_1/d\tau$ with C_L shown in Fig. 13(f) is qualitatively similar. To eliminate the effect of the two dominant
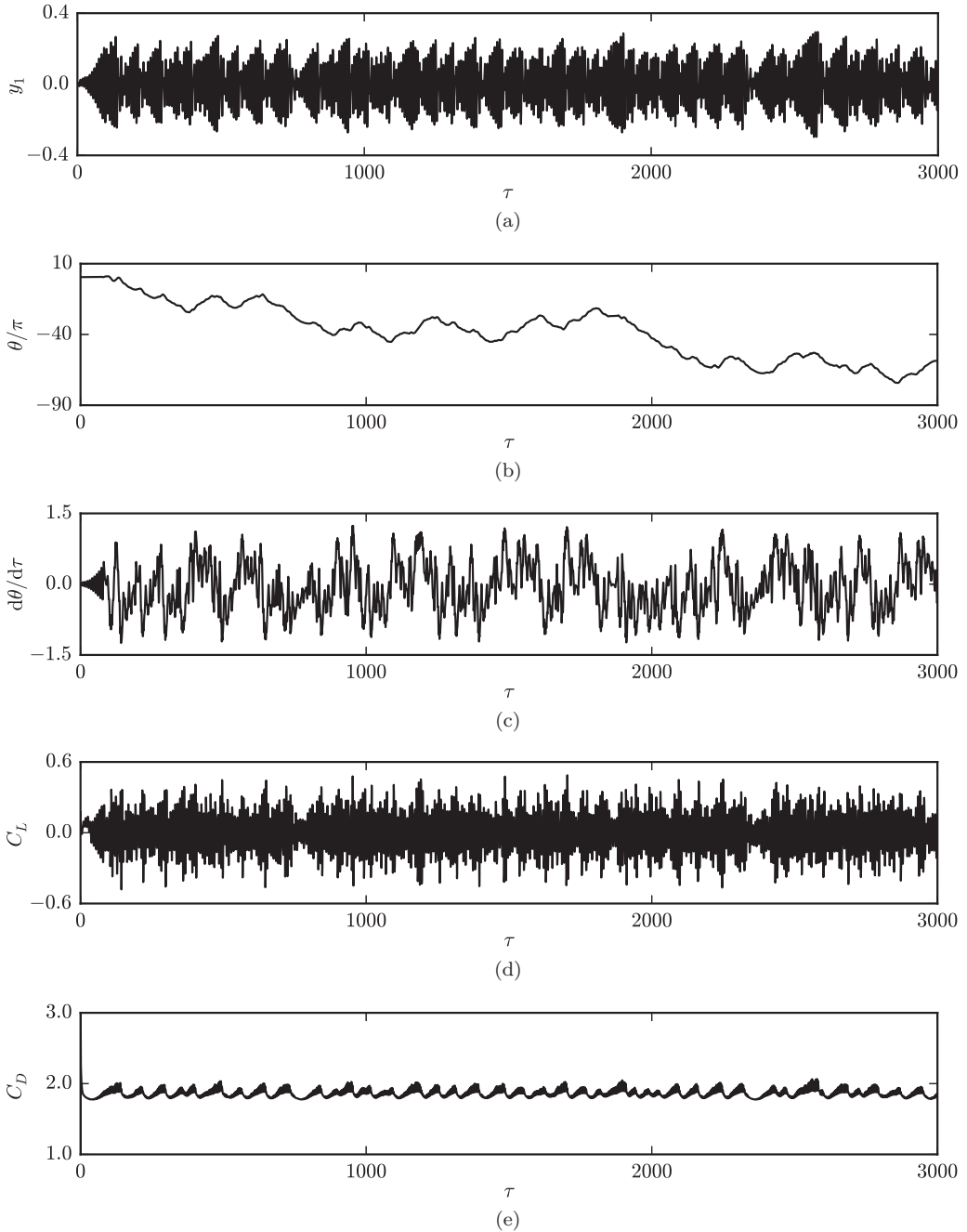
FIG. 11. Time series for the FDC solution found with inlet transient C at Re = 31 and $1/g_n^* = 0.28$: (a) cylinder displacement, (b) NES angular position, (c) NES angular velocity, (d) lift coefficient, and (e) drag coefficient.

frequencies in the correlation plots, we apply a first-order Butterworth band-stop filter with lower and upper critical frequencies $0.05D/U$ and $0.6D/U$, respectively, to the time series of $dy_1/d\tau$, C_L, $v_{x,P}$, $v_{y,P}$, $v_{x,Q}$, and $v_{y,Q}$. In contrast to Figs. 13(a)–13(f), Figs. S8(a)–S8(f) [29] show that the
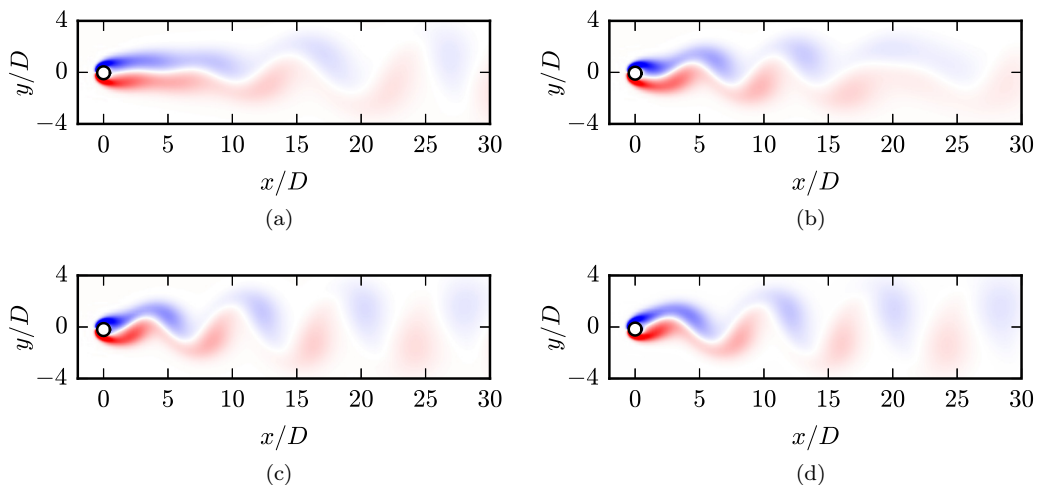
FIG. 12. Spanwise vorticity for the NES-equipped FDC solution found with inlet transient C at Re = 31 and $1/g_n^* = 0.28$, at (a) $\tau = 766.8$, (b) $\tau = 1532.2$, and (c) $\tau = 1890.8$, and (d) NES-less VIV for the same parameters and the same phase of cylinder motion as in panel (c).
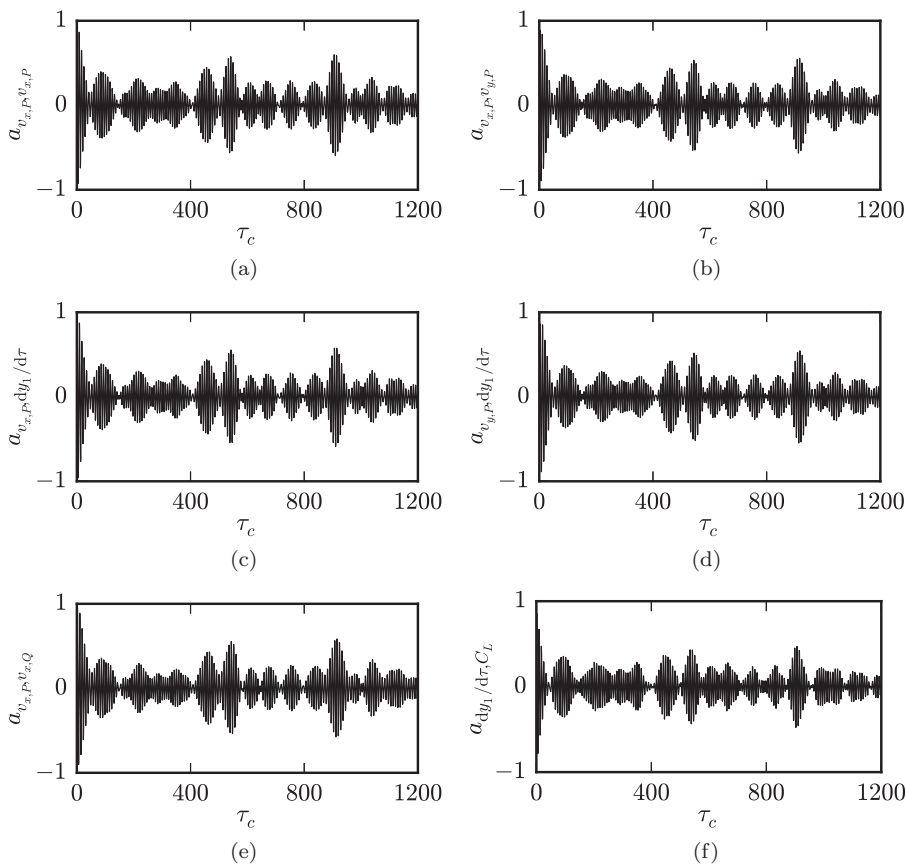

FIG. 13. For the FDC solution found with inlet transient C at Re = 31 and $1/g_n^* = 0.28$, (a) autocorrelation of $v_{x,P}$, and cross correlations of (b) $v_{x,P}$ and $v_{y,P}$, (c) $v_{x,P}$ and $dy_1/d\tau$, (d) $v_{y,P}$ and $dy_1/d\tau$, (e) $v_{x,P}$ and $v_{x,Q}$, and (f) $dy_1/d\tau$ and C_L.

autocorrelations of the filtered signals are virtually zero after about 30 time units, which corresponds to approximately five shedding cycles.

Cursory inspection of the time series for θ (Fig. S9 [29]) shows that the NES mass does not have a strong preference for any particular position (e.g., $\theta = n\pi$ for any integer n). This is more clearly seen using the cumulative distribution function

$$F_\theta(\phi) = P(\theta \bmod 2\pi \leqslant \phi), \quad \phi \in [-\pi, \pi), \tag{6a}$$

and probability density function

$$f_\theta(\phi) = dF_\theta(\phi)/d\phi, \quad \phi \in [-\pi, \pi) \tag{6b}$$

where $P(X_i)$ is the probability that the variable X assumes the value X_i. For Re = 31, $1/g_n^* = 0.28$, and inlet transient C, the NES mass has only a very weak preference for $\theta = 0$ or π (see Figs. S10(a) and S10(b) [29]). This preference persists regardless of the sampling window used in the time series, and regardless of whether the PDF is computed by differentiation of the distribution function, or by a "binning" approach (Figs. S10(c)–10(f) [29]). The PDF is an approximately even function of θ, with minima near $\pm\pi/2$.

The CDF and PDF of $d\theta/d\tau$ at the times when θ crosses through an integer multiple of π show that there is a minimum nonzero value of $|d\theta/d\tau|$ (Figs. S11(a) and S11(b) [29]). Comparison to the CDF and PDF when the values of $d\theta/d\tau$ are additionally conditioned on the requirement that the NES mass was displaced by at least 0.1 (rad) since the previous zero crossing, to eliminate the effect of "jitter" near integer multiples of π (Figs. S11(c) and S11(d) [29]), shows that the crossings having the smallest values of $|d\theta/d\tau|$ are "jittering" near integer multiples of π. No instances were found in which θ and $d\theta/d\tau$ simultaneously vanished. (If this happened, Eq. (2b) shows that the NES mass would come to rest, and Eq. (2a) shows that the solution would be identical to standard VIV thereafter.) It is clear that there is a threshold value of $|d\theta/d\tau| \approx 0.1$ for "jitterless" crossings of $\theta = n\pi$. The explanation is that if $|d\theta/d\tau|$ is sufficiently small when $\theta = n\pi$, then "capture" by a VIV or SSMC solution (with no rotation of the NES mass) is possible if the small amount of rotational kinetic energy can be dissipated. In that case, the long-time solution would not be chaotic.

To further characterize the fully developed chaotic solution, we estimate the correlation dimensions d_{corr} of y_1 and C_L using the algorithm of Grassberger and Procaccia [39], implemented by Hegger $et~al.$ [40]. We compute the correlation sum $C_m(\sigma)$ over a range of scales σ for several values of the embedding dimension m. Convergence of d_{corr} is established when for sufficiently large m, the slope of $\log C_m(\sigma)$ versus $\log \sigma$ becomes independent of m and σ over a relatively broad range of σ. For such a range, $C_m(\sigma)$ scales like $\sigma^{d_{\text{corr}}}$.

We apply this approach at Re = 31 and $1/g_n^* = 0.28$ with inlet transient C [Figs. 11(a) and 11(d)]. We discard the initial portion of the time series ($0 \leqslant \tau \leqslant 70$), use 500 points per convective time unit (about 3000 points per nominal shedding cycle), a time delay chosen in the standard way (here, 1046 sampled points), and a Theiler window parameter corresponding to 10 000 sampled points. Least-squares lines fitted to C_m over the same intermediate range of σ (roughly $10^{-3} \leqslant \sigma \leqslant 10^{-2}$) used by Tumkur $et~al.$ [23] show that as m increases, the limiting slopes of $\log C_m(\sigma)$ versus $\log \sigma$ for y_1 and C_L are 3.46 and 3.50, respectively, consistent with the dimension of 3.2 found by Tumkur $et~al.$ [23] for a different chaotic solution at Re = 100 with other values of $1/g_n^*$ and the NES parameters. As discussed by those authors, such relatively low values for the correlation dimension are consistent with expectations for low- and intermediate-Re flows with two additional degrees of freedom (rectilinear cylinder motion and NES mass rotation) and are comparable to the fractal dimensions of 2.48, 3.10, and 4.65 computed for a temporally chaotic two-dimensional flow past a NACA 0012 airfoil at Re = 1600, 2000, and 3000, respectively [41].

2. Steplike chaotic (SLC) solutions

For Re = 36, $1/g_n^* = 0.17$ (the parameters for which results were presented above for the SSMC and PPUR solutions), and inlet transient B, Figs. 14(a)–14(e) and Movie 7 [29] show that the
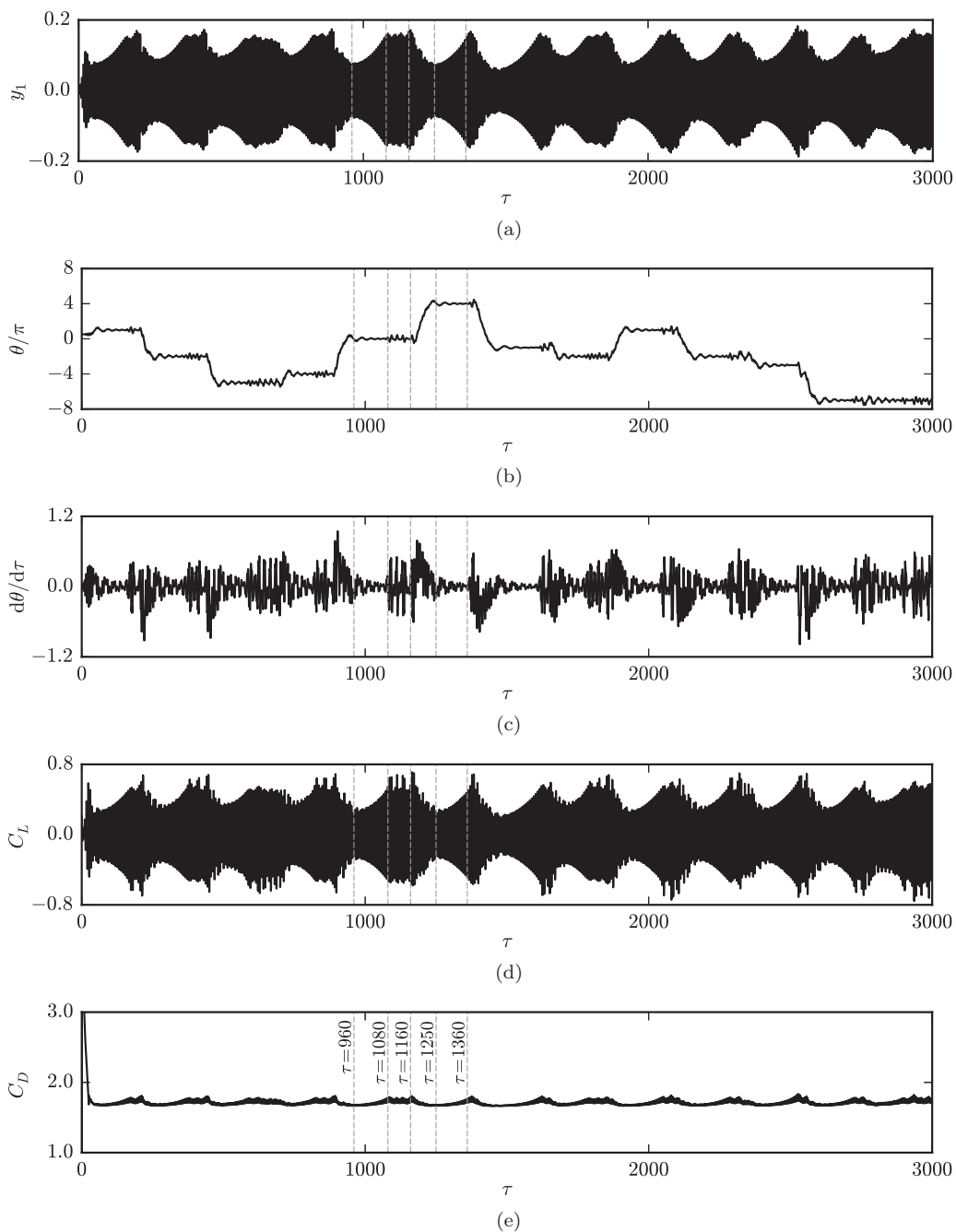
FIG. 14. Time series for the SLC solution found with inlet transient B at Re = 36 and $1/g_n^* = 0.17$: (a) cylinder displacement, (b) NES angular position, (c) NES angular velocity, (d) lift coefficient, and (e) drag coefficient.

long-time solution is characterized by a succession of intervals (e.g., $960 < \tau < 1080$) during which the oscillation amplitudes of y_1, C_L, and C_D monotonically grow, the NES mass nearly comes to rest at $\theta = n\pi$ ($n = 0$ for $960 < \tau < 1080$), and the solution appears to, but does not, approach the standard VIV solution. As the amplitudes of y_1 and C_L near their maximum values (e.g., near
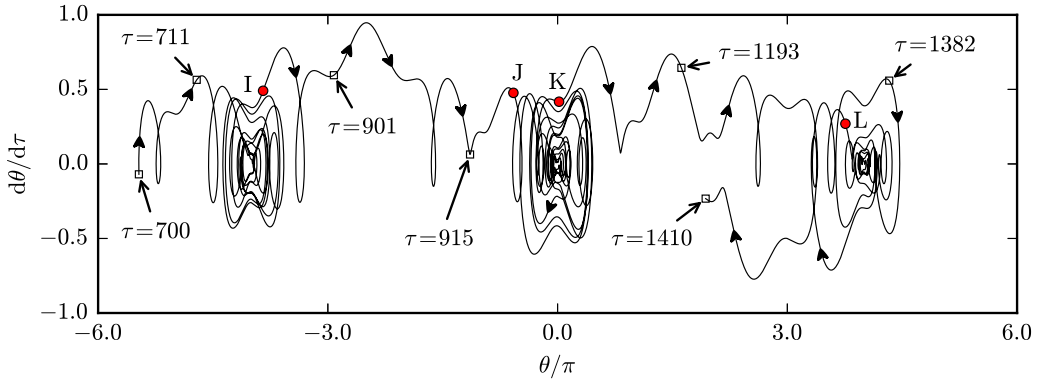
FIG. 15. Detail, from $\tau = 700$ to $\tau = 1410$, of the trajectory, in a two-dimensional projection of the phase space, for the SLC solution found with inlet transient B at Re = 36 and $1/g_n^* = 0.17$; closed circles at I and J denote the approximate times at which the first 1:1 resonance capture begins and ends ($\tau = 892.5$ and 922, respectively), while closed circles at K and L refer to the corresponding times ($\tau = 1180.5$ and 1224.5, respectively) for the second capture. Open squares denote points at specified values of τ.

$\tau = 1080$), there is a rapid onset of large-amplitude oscillations of the NES mass, marking the end of linear growth of y_1 and C_L, and the onset of temporal chaos. This intermittent bursting manifests itself in broadband frequency content of the wavelet spectra for y_1, $\sin \theta$, and C_L, shown in Figs. S12(a)–S12(c) [29]. This chaotic episode, whose duration varies from one cycle to the next, ends with a sudden reduction in oscillation amplitudes for y_1, C_L, and C_D (nearly twofold for y_1 and C_L between $\tau = 1160$ and $\tau = 1250$ in Figs. 14(a) and 14(d), respectively). The NES mass concomitantly executes a large-amplitude, predominantly counterclockwise motion, and rapidly jumps, in what we refer to below as a 1:1 resonance capture, from $n\pi$ to about $m\pi$, where n and m are distinct integers [Fig. 14(b)]. While the angular position of the NES mass slowly approaches $m\pi$ ($m = 4$ for $1250 < \tau < 1360$), the amplitudes of y_1 and C_L begin to grow rapidly, and the previously described behavior starts anew. The steplike nature of the time series for θ corresponds to these successive jumps from $n\pi$ to $m\pi$, where $|n - m| \leqslant 4$ in the cases examined.

The corresponding wavelet spectra (Figs. S12(a)– S12(c) [29]) for y_1, $\sin \theta$, and C_L exhibit several notable features. The spectrum for y_1 shows that the long-time cylinder response is exclusively at the Strouhal frequency during the intervals of linear growth of y_1 and C_L (e.g., for $1250 \leqslant \tau \leqslant 1360$ and for $1480 \leqslant \tau \leqslant 1600$), and predominantly at the Strouhal frequency otherwise, with a broadband contribution evidencing temporal chaos. Identical conclusions can be drawn from the spectrum of C_L. On the other hand, the spectrum of $\sin \theta$ exhibits no dominant frequency and is predominantly broadband, except for intervals during which the NES mass nearly comes to rest after a jump. As discussed above, each such interval features sudden, predominantly unidirectional motion of the NES mass, immediately followed by a much quieter interval.

The wavelet spectrum of $\sin \theta$ (Fig. S12(b) [29]) shows that during each angular jump of the NES mass shown in Fig. 14(b), there is a dominant frequency close to St, which slowly and slightly decays as the NES mass approaches an integer multiple of π. This strongly suggests that each jump in θ is the manifestation of a transient 1:1 resonance capture during which energy transfer from the cylinder to the NES mass occurs, leading to a rapid decrease in the amplitude of y_1. Each such event is followed by a prolonged interval during which the NES mass becomes nearly motionless near $\theta = n\pi$, corresponding to escape from the state of 1:1 resonance. To illustrate this point, Fig. 15 shows the trajectory of the NES mass in the two-dimensional projection ($\theta, d\theta/d\tau$) of the phase space for a time window during which several such 1:1 transient resonance captures (two in the present case) successively occur.

To establish the temporally chaotic nature of the steplike solution at Re $= 36$ and $1/g_n^* = 0.17$ with inlet transient B, we compute the correlation dimension of the attractor. We use $100 \leqslant \tau \leqslant 3000$, 500 points per convective time unit, a time delay corresponding to 833 sampled points, and a Theiler window parameter corresponding to 10 000 sampled points. For y_1 and C_L, the correlation dimension d_{corr} approaches limiting values of 2.64 and 2.62, respectively, as m increases. These values are measurably lower than those determined above for the FDC solution.

3. Slowly decaying cycle (SDC) solutions

For Re $= 46$, $1/g_n^* = 0.15$ and inlet transient B, Figs. 16(a)–16(e) and Movie 8 [29] show that the long-time solution is characterized by successive cycles of regular motion interrupted by chaotic bursts. During each interval of regular motion, the oscillation amplitudes of y_1, C_L, and C_D slowly decrease, and the NES mass executes nearly unidirectional rotational motion. At the end of each such SDC, the cylinder has almost come to rest. This is followed by a short interval during which the cylinder remains nearly motionless, the angular velocity of the NES mass decays considerably, the oscillation amplitude of C_L decreases precipitously (to below 0.04), and C_D is nearly constant. This strongly suggests that, during each such interval, the trajectory approaches an SSMC state (in which the cylinder and NES mass are motionless, with no lift and constant drag). If an SSMC solution was indeed reached, its stability would depend on the angular position of the NES mass, as discussed in Sec. III B.

However, as $|d\theta/d\tau|$ decreases toward zero, the oscillation amplitudes of y_1 and C_L grow. This leads to transfer of kinetic energy from rectilinear cylinder motion to NES mass rotation and ultimately gives rise to large-amplitude oscillations of the latter. This rapid linear growth of θ ushers in an interval of transient chaos, the duration of which varies among the SDCs within a single time series. For Re $= 46$ and $1/g_n^* = 0.15$, the trajectory settles into a new slowly decaying cycle, strongly suggesting that the "intermittently chaotic" slowly decaying solution is not part of a longer initial transient, but, rather, is a stable attractor for the present combination of parameters.

A remarkable feature of this slowly decaying solution is the striking change in wake structure at the end of each SDC and immediately thereafter. As discussed above, each SDC ends with a dramatic diminution of the amplitudes of y_1, C_L, and C_D, followed by a brief interval during which the solution appears to approach an SSMC solution. This transition from a large-amplitude VIV-like state to a nearly SSMC state is accompanied by slow, yet considerable, elongation of the attached vorticity, as shown in Movie 8 [29] for the entire computation. Movie 9 [29] shows that, for a large fraction of the first SDC ($200 < \tau < 765$), the wake is qualitatively similar to standard VIV (compare to Movie 10 [29] at the same Re and $1/g_n^*$), and that it is not until $\tau \approx 660$, when the amplitude of y_1 rapidly drops, that significant wake elongation begins. Still later, the attached vorticity is elongated to about $10D$ (see Movie 9 [29] at $\tau = 757.2$). Elongation and symmetrization of the wake continue as the cylinder and NES mass become nearly motionless, C_L approaches zero, and C_D becomes nearly constant. The attached vorticity elongates beyond $30D$ (see $\tau = 850$ in Movie 9 [29]), corresponding to a nearly symmetric vorticity distribution, with slight waviness attributable to small residual oscillatory motion of the cylinder.

We conjecture that the instability that develops following the spectacular elongation and nearly complete symmetrization of the vorticity distribution, and which starts the trajectory on its path toward temporal chaos, has its origin in the following. Near the "quietest" time in one cycle [e.g., over $800 < \tau < 846$ in Figs. 16(a)–16(e)], $|d\theta/d\tau|$ decreases while θ passes through $n\pi$, but this clearly does not lead to θ and $d\theta/d\tau$ vanishing asymptotically, and "capture" by a VIV or SSMC solution. Instead, an instability leading to another cycle of chaotic motion develops. Figure 2 shows that the point Re $= 46$, $1/g_n^* = 0.15$ is on the unstable side of the NES-equipped (with $\varepsilon_p \sin^2 \theta_s = \varepsilon_p$) and NES-less (with $\varepsilon_p \sin^2 \theta_s = 0$) stability boundaries, for which the codimension-two points are at $1/g_n^* = 0.119$ and 0.140, respectively. Thus, we expect that no SSMC solution (regardless of θ_∞) will be linearly stable.
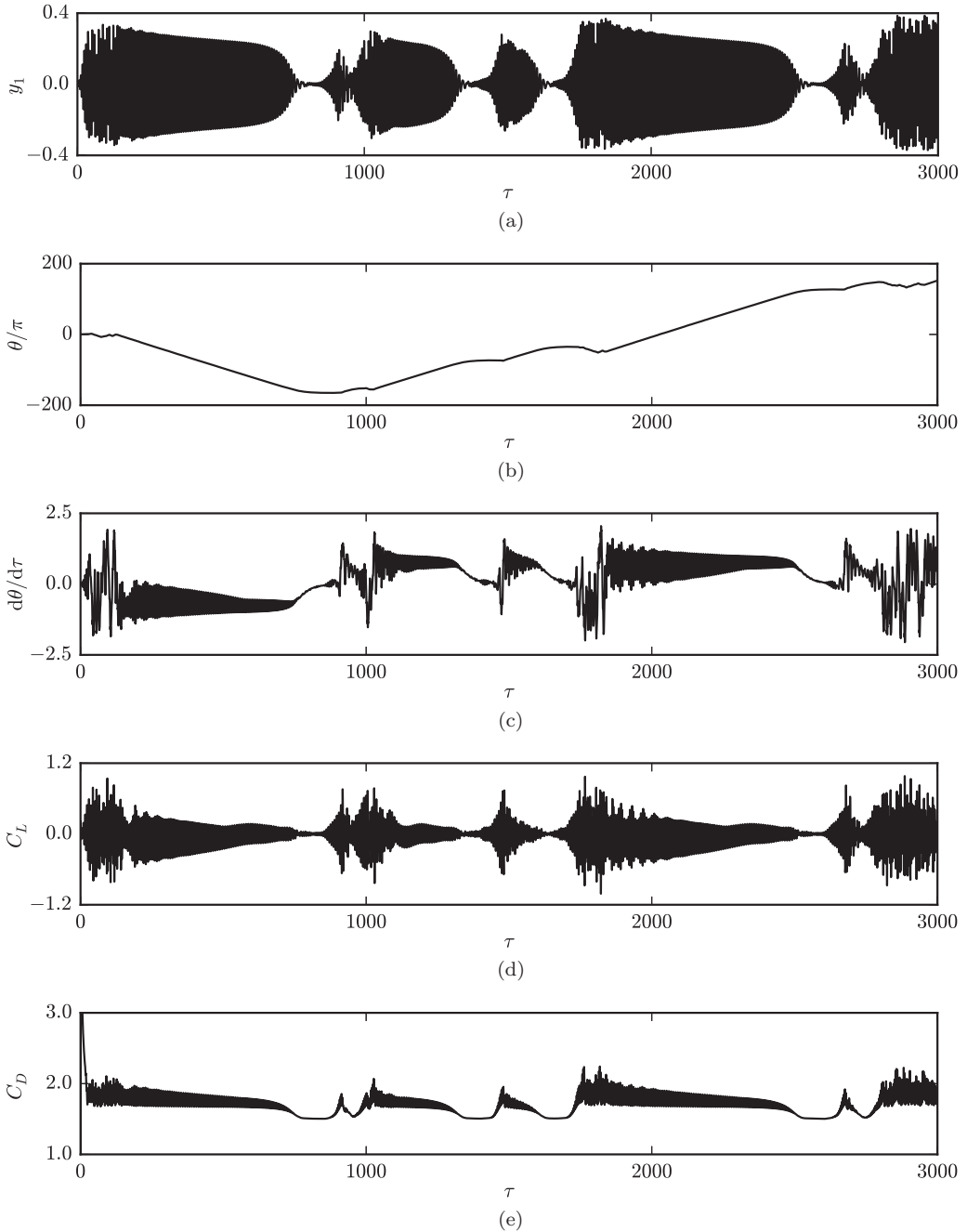
FIG. 16. Time series for the SDC solution found with inlet transient B at Re $= 46$ and $1/g_n^* = 0.15$: (a) cylinder displacement, (b) NES angular position, (c) NES angular velocity, (d) lift coefficient, and (e) drag coefficient.

Because the SDC solution lies on a chaotic attractor, no two slowly decaying cycles in a given time series are identical in duration or mean amplitude. Of the four SDCs shown in Figs. 16(a)–16(e), two (corresponding to approximately $200 < \tau < 765$ and $1870 < \tau < 2520$) extend over intervals significantly longer than the other two (covering approximately $1100 < \tau < 1350$ and

$1510 < \tau < 1640$). Figure 16(a) shows that the oscillation amplitude of y_1 decreases approximately linearly during the first portion of each SDC (e.g., for $200 < \tau < 600$, during which the amplitude of y_1 drops by about 27%), after which it decays much more rapidly in the latter portion of the cycle (e.g., $660 < \tau < 765$ for the first SDC, during which the amplitude of y_1 drops by about 88%). During the intervals of slow decay, strong modulation is seen in C_L and $d\theta/d\tau$, with that of the former exhibiting a strong departure from up-down symmetry. Modulation in the oscillation of C_L is not reflected in the cylinder motion but does seem to affect modulation of $d\theta/d\tau$, as evidenced by the inflection near the minima of $|d\theta/d\tau|$ at about $\tau = 580$ and $\tau = 2330$, accompanied by a similar inflection near the minima of C_L. Finally, as required by invariance of Eqs. (2a) and (2b) under a sign change in θ, the direction of rotation of the NES mass has no influence on the flow. This is reflected in the qualitatively very similar wave forms of the lift coefficient for the first ($200 < \tau < 765$) and last ($1870 < \tau < 2520$) SDCs in Fig. 16(d), with the NES mass rotating predominantly counterclockwise and clockwise during the former and latter periods, respectively.

Wavelet spectra for y_1, $\sin\theta$, and C_L (Figs. S13(a)–S13(c) [29]) show that, during each SDC, the response is predominantly at a frequency near the Strouhal frequency, with higher harmonics being weak and present during only part of each SDC. (This is particularly clear in the time series shown in Movie 9 [29] for the first SDC.) During the chaotic bursts, there is no discernible dominant frequency, indicative of a broadband response.

To confirm the chaotic nature of the long-time slowly decaying solution, we compute the correlation dimension of the attractor as described earlier, discarding the portion of the time series corresponding to $\tau < 50$. As the embedding dimension m increases, the correlation dimension approaches limiting values of 2.50 and 2.55 for y_1 and C_L, respectively, comparable to those obtained for the steplike chaotic solution described above. In contrast, application of this procedure to the first SDC ($200 < \tau < 765$) yields correlation dimensions of 2.28 and 2.24 for y_1 and C_L, respectively, slightly smaller than those obtained for the longer time series. For the same Re and $1/g_n^*$ values, Figs. S14(a)–S14(e) [29] show that halving the time-step size and increasing the polynomial order produces results that are qualitatively similar to those shown in Figs. 16(a)–16(e). This supports the statement made earlier that the statistics of the reported chaotic long-time solutions are insensitive to the details of the discretization.

A slowly decaying solution of similar type was found by Tumkur *et al.* [23] at higher Re ($60 \leqslant$ Re $\leqslant 120$) and with different NES parameters. For $m^* = 10$, $1/g_n^* = 0.059$, Re $= 100$, $\varepsilon_p = 0.3$, $\bar{r}_0 = 0.5$, $\zeta = 0.3395$, $\theta_i = \pi/2$, and inlet transient E (uniform flow), those authors found a similar slowly decaying solution, with elongation of the attached vorticity to a downstream position as much as $9.5D$ aft of the cylinder center. In contrast to the Re $= 46$ case described above, the intermittently bursting solution found by Tumkur *et al.* [23] features a dominant frequency that continuously decreases as each SDC progresses, falling well below St before each burst into chaos. This mechanism was attributed to an added-mass effect induced by the presence of the NES mass. Another noteworthy difference is that all SDCs of the slowly decaying solution found by Tumkur *et al.* [23] have similar durations.

V. DISCUSSION

A. Overview of multiplicity and the phase diagram

Although rigorous demonstration that any of the unsteady long-time solutions reported in Sec. IV are stable or attracting is beyond the scope of this work, the facts that they are found at Reynolds numbers where flow past a vibrating circular cylinder is thought to be two dimensional, that they persist over hundreds of shedding cycles, and that they appear to be robust with respect to the computational parameters strongly suggest that they are locally stable or attracting, within the class of two-dimensional solutions [3]. This also suggests that for combinations of Re and $1/g_n^*$ for which two or more long-time solutions coexist, "mode switching" of the trajectory between them can
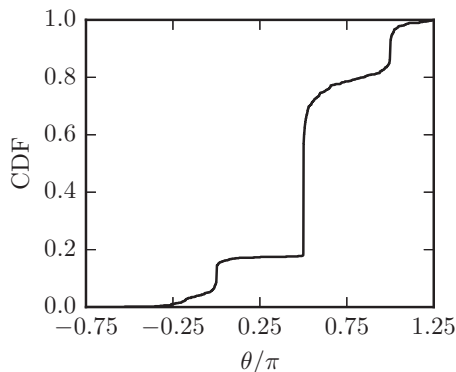
FIG. 17. CDF of θ_∞ for all SSMC solutions found.

occur only as the result of strong external disturbances. This question is worthy of investigation but beyond the scope of the present work.

Figure 2 shows that for intermediate Re, there is a large portion of the Re-$1/g_n^*$ plane in which two or more long-time solutions coexist and no solution is globally attracting. For one combination of the parameters (Re = 37, $1/g_n^* = 0.17$), we find two periodic solutions and a chaotic solution coexisting with more than one steady solution. For a number of other combinations of Re and $1/g_n^*$, we find two distinct unsteady solutions (both periodic, one periodic and one quasiperiodic, one periodic and one chaotic, one quasiperiodic and one chaotic, or both chaotic), in most cases coexisting with one or more steady solutions. For no Re-$1/g_n^*$ combination do we find five or more long-time solutions, and in no case are more than three unsteady. No aperiodic solutions are found for $1/g_n^* > 0.38$.

As discussed in Sec. I, multiple long-time solutions of the Navier-Stokes equations have been found before. In the majority of the situations in which multiplicity has been found, the flow is driven by rotation of an infinite plane or by rotation of one or both members of a pair of infinite planes (see Refs. [1,2], and references cited therein), and all of the flows are either steady or time periodic. For pipe flow, the steady Poiseuille solution is linearly stable at Re values well above the experimentally observed critical Re associated with finite-amplitude instability [42], so that the "base flow" and turbulence coexist over a wide range of Re. For pipe flow and plane Couette flow [43], intermittency, in which laminar and turbulent flow alternate in time at a particular streamwise location, have also been observed over a range of conditions. But no previous case of which we are aware gives rise to the degree of multiplicity found here, in which as many as three unsteady long-time solutions (including one or more aperiodic solutions) coexist with one or more steady solutions in a laminar flow.

As discussed by Tumkur *et al.* [23], the stability boundaries shown in Fig. 2 demonstrate that below the fixed-cylinder critical value Re$_{\text{fixed}} \approx 46$, an NES can stabilize the $\theta_s = \pi/2$ SSMC solution, in the sense that there are combinations of Re and $1/g_n^*$ for which this SSMC solution is unstable absent an NES and stable with an NES. The stability boundaries also show that in the same range of Re, an NES with $\theta_s = \pi/2$ can destabilize the SSMC solution. This raises the question of how an NES might be used at higher Re, to not only change the amplitude of VIV but also to completely suppress VIV. If one thinks of the VIV suppression "design" problem as one in which the goal is to use the NES to "bleed off" energy from incipient rectilinear motion, then one approach is to place the rotating mass at $\theta = \pi/2$, where Eqs. (2a) and (2b) show that "maximum coupling" is obtained in the case of small-amplitude oscillations.

Finally, Fig. 17 shows the cumulative probability distribution function of final values of the angular position of the NES mass for all combinations of Re, $1/g_n^*$ and inlet transient for which an SSMC solution was found. It is not surprising that there is a large concentration near $\theta = \pi/2$,

where all of the simulations begin, and many end. However, there are also large concentrations near integer multiples of π. These correspond to solutions in which (a) the inlet transient excited significant cylinder motion, (b) the NES ultimately bled off kinetic energy from the rectilinear motion of the cylinder, and (c) in accomplishing that, the NES mass was "entrained" into a final angular position that is an integer multiple of π.

B. Experimental considerations

Finally, the issue arises as to how our predictions can be confirmed experimentally. There are three key questions. First, how can an experiment be set up? Second, will three-dimensional effects render the two-dimensional analysis moot? Third, what is the importance of nonlinearity?

Experimental realization, including a detailed analysis of a distributed rotating mass dynamically equivalent to the point-mass model described here in Sec. II A, was discussed by Tumkur *et al.* [23]. We pointed out there that constraints on the radial extent of the rotator (associated with either large values of $\bar{r}_0$ or the maximum density of available materials) can be overcome by placing the rotating mass outside the spanwise extent of the flow. We note here that if the rotator is placed outside of the flow domain, one need not use very dense materials (e.g., tungsten), because the spanwise extent of the rotating mass can be made as large as needed. This is a simple consequence of the fact that the rotating and nonrotating masses are characterized on a per-unit-length basis, where the relevant length is the spanwise extent of the flow. So placing the rotating mass (or for that matter, some of the nonrotating mass) beyond the spanwise boundaries of the flow increases the mass, while leaving the (flow) length unchanged.

Three-dimensionality can become an issue in two ways. First, for a fixed cylinder, even a slightly three-dimensional geometry (e.g., any finite-span cylinder) can give rise to oblique shedding [44]. While this is not well understood in the context of flow-induced vibration, it is clear that the effects can be reduced by use of a large-aspect-ratio cylinder. To assess the significance of three-dimensional geometries would require computation of three-dimensional time-periodic base flows and Floquet analysis of their stability, which is beyond the scope of the present work. Second, there is the potential for three-dimensional instability in a strictly two-dimensional base flow [45,46]. Fortunately, work by Leontini *et al.* [46] strongly suggests that two-dimensional flow past a circular cylinder undergoing either transverse VIV or forced transverse oscillation becomes unstable with respect to three-dimensional disturbance at Re above the known fixed-cylinder critical value of 190 [45], far beyond the range considered here.

As for nonlinearity, we note that our results were obtained in simulations of the fully nonlinear governing equations, in which the initial-value problem was solved using disturbances of significant magnitude in the inlet transients [Eqs. (3a)–(3d)]. No linearization was performed, and the allowance for large disturbances strongly suggests that the results should be relatively robust with respect to typical disturbances in laboratory facilities.

VI. CONCLUSION

For a linearly sprung circular cylinder in cross flow at Re < 50, equipped with a nonlinear energy sink consisting of a rotating mass and a linear damper, we found that as many as three distinct unsteady long-time solutions (two time-periodic solutions and one temporally chaotic solution) and a steady, symmetric, motionless-cylinder solution can coexist for a single combination of Re, dimensionless spring constant, ratio of cylinder density to fluid density, and parameters characterizing the rotating mass and its damper. For a number of other combinations of Re and $1/g_n^*$ (with the other parameters unchanged), we find two distinct unsteady solutions (both periodic, one periodic and one quasiperiodic, one periodic and one chaotic, one quasiperiodic and one chaotic, or both chaotic), in most cases coexisting with one or more steady solutions. The discovery of this unprecedented degree of multiplicity in a range of Re (15 < Re < 50) far removed from any expected three-dimensionality is significant because it facilitates high-fidelity computations that

can delineate the structure of the basins of attraction in the initial condition space (or the space of inlet transients). Understanding solution multiplicity is especially important to studies of noise- and disturbance-induced transition between attracting solutions and to flow control. All of the results are obtained for a density ratio of ten, thus allowing experiments to be performed in water or other liquids, without the cylinder extending beyond the span of the flow.

[1] P. J. Zandbergen and D. Dijkstra, Von Kármán swirling flows, Annu. Rev. Fluid Mech. **19**, 465 (1987).

[2] M.-J. Zhang and W.-D. Su, Exact solutions of the Navier-Stokes equations with spiral or elliptical oscillation between two infinite planes, Phys. Fluids **25**, 073102 (2013).

[3] Navrose and S. Mittal, A new regime of multiple states in free vibration of a cylinder at low Re, J. Fluids Struct. **68**, 310 (2017).

[4] Navrose and S. Mittal, The critical mass phenomenon in vortex-induced vibration at low Re, J. Fluid Mech. **820**, 159 (2017).

[5] B. Eckhardt, T. M. Schneider, B. Hof, and J. Westerweel, Turbulence transition in pipe flow, Annu. Rev. Fluid Mech. **39**, 447 (2007).

[6] M. M. Chen and J. A. Whitehead, Evolution of two-dimensional periodic Rayleigh convection cells of arbitrary wave numbers, J. Fluid Mech. **31**, 1 (1968).

[7] F. H. Busse, Non-linear properties of thermal convection, Rep. Prog. Phys. **41**, 1929 (1978).

[8] R. M. Clever and F. H. Busse, Steady and oscillatory bimodal convection, J. Fluid Mech. **271**, 103 (1994).

[9] R. M. Clever and F. H. Busse, Hexagonal convection cells under conditions of vertical symmetry, Phys. Rev. E **53**, R2037 (1996).

[10] D. Coles, Transition in circular Couette flow, J. Fluid Mech. **21**, 385 (1965).

[11] J. E. Burkhalter and E. L. Koschmieder, Steady supercritical Taylor vortex flow, J. Fluid Mech. **58**, 547 (1973).

[12] R. C. DiPrima and H. L. Swinney, Instabilities and transition in flow between concentric rotating cylinders, in *Hydrodynamic Instabilities and the Transition of Turbulence*, edited by H. L. Swinney and J. P. Gollub (Springer Verlag, Heidelberg, 1985), pp. 139–180.

[13] T. B. Benjamin and T. Mullin, Notes on the multiplicity of flows in the Taylor experiment, J. Fluid Mech. **121**, 219 (1982).

[14] S. G. Huisman, R. C. A. van der Veen, C. Sun, and D. Lohse, Multiple states in highly turbulent Taylor-Couette flow, Nat. Commun. **5**, 3820 (2014).

[15] R. T. Goodwin and W. R. Schowalter, Interactions of two jets in a channel: Solution multiplicity and linear stability, J. Fluid Mech. **313**, 55 (1996).

[16] R. D. Simitev and F. H. Busse, Bistable attractors in a model of convection-driven spherical dynamos, Phys. Scr. **86**, 018409 (2012).

[17] E. W. Bolton and A. Firoozabadi, Numerical modeling of temperature and species distributions in hydrocarbon reservoirs, J. Geophys. Res.: Solid Earth **119**, 18 (2014).

[18] R. M. Fearn, T. Mullin, and K. A. Cliffe, Nonlinear flow phenomena in a symmetric sudden expansion, J. Fluid Mech. **211**, 595 (1990).

[19] M. Wegener, M. Kraume, and A. R. Paschedag, Terminal and transient drop rise velocity of single toluene droplets in water, AIChE J. **56**, 2 (2010).

[20] R. F. Engberg and E. Y. Kenig, An investigation of the influence of initial deformation on fluid dynamics of toluene droplets in water, Int. J. Multiphase Flow **76**, 144 (2015).

[21] B. Jhaveri and G. M. Homsy, Randomly forced Rayleigh-Bénard convection, J. Fluid Mech. **98**, 329 (1980).

[22] T. Mullin, Experimental studies of transition to turbulence in a pipe, Annu. Rev. Fluid Mech. **43**, 1 (2011).

[23] R. K. R. Tumkur, A. J. Pearlstein, A. Masud, O. V. Gendelman, A. B. Blanchard, L. A. Bergman, and A. F. Vakakis, Effect of an internal nonlinear rotational dissipative element on vortex shedding and vortex-induced vibration of a sprung circular cylinder, J. Fluid Mech. **828**, 196 (2017).

[24] O. V. Gendelman, G. Sigalov, L. I. Manevitch, M. Mane, A. F. Vakakis, and L. A. Bergman, Dynamics of an eccentric rotational nonlinear energy sink, J. Appl. Mech. **79**, 011012 (2012).

[25] G. Sigalov, O. V. Gendelman, M. A. Al-Shudeifat, L. I. Manevitch, A. F. Vakakis, and L. A. Bergman, Alternation of regular and chaotic dynamics in a simple two-degree-of-freedom system with nonlinear inertial coupling, Chaos **22**, 013118 (2012).

[26] G. Sigalov, O. V. Gendelman, M. A. Al-Shudeifat, L. I. Manevitch, A. F. Vakakis, and L. A. Bergman, Resonance captures and targeted energy transfers in an inertially coupled rotational nonlinear energy sink, Nonlinear Dyn. **69**, 1693 (2012).

[27] G. B. Schubauer and H. K. Skramstad, Laminar-boundary-layer oscillations and transition on a flat plate, NACA Report 909, National Advisory Committee for Aeronautics, Washington, D.C., 1948.

[28] H. Fasel, Investigation of the stability of boundary layers by a finite-difference model of the Navier-Stokes equations, J. Fluid Mech. **78**, 355 (1976).

[29] See Supplemental Material at http://link.aps.org/supplemental/10.1103/PhysRevFluids.4.054401 for supplemental movies, tables, and figures referenced in the paper.

[30] P. F. Fischer, J. W. Lottes, and S. G. Kerkemeier, Nek5000 http://nek5000.mcs.anl.gov.

[31] S. T. Trickey, L. N. Virgin, and E. H. Dowell, The stability of limit-cycle oscillations in a nonlinear aeroelastic system, Proc. Royal Soc. London, Ser. A **458**, 2203 (2002).

[32] K. Czolczynski, P. Perlikowski, A. Stefanski, and T. Kapitaniak, Synchronization of slowly rotating pendulums, Int. J. Bifurcation Chaos **22**, 1250128 (2012).

[33] D. Lyons, J. M. Mahaffy, S. Wang, A. Palacios, and V. In, Geometry of basins of attraction and heteroclinic connections in coupled bistable systems, Int. J. Bifurcation Chaos **24**, 1430029 (2014).

[34] M. O. Williams, I. G. Kevrekidis, and C. W. Rowley, A data-driven approximation of the Koopman operator: Extending dynamic mode decomposition, J. Nonlinear Sci. **25**, 1307 (2015).

[35] S. Zhou, J. Cao, D. J. Inman, J. Lin, and D. Li, Harmonic balance analysis of nonlinear tristable energy harvesters for performance enhancement, J. Sound Vib. **373**, 223 (2016).

[36] J. D. Skufca, J. A. Yorke, and B. Eckhardt, Edge of Chaos in a Parallel Shear Flow, Phys. Rev. Lett. **96**, 174101 (2006).

[37] B. J. A. Zielinska and J. E. Wesfreid, On the spatial structure of global modes in wake flow, Phys. Fluids **7**, 1418 (1995).

[38] Y.-C. Lai and T. Tél, *Transient Chaos: Complex Dynamics on Finite Time Scales* (Springer Verlag, New York, 2011).

[39] P. Grassberger and I. Procaccia, Characterization of Strange Attractors, Phys. Rev. Lett. **50**, 346 (1983).

[40] R. Hegger, H. Kantz, and T. Schreiber, Practical implementation of nonlinear time series methods: The TISEAN package, Chaos **9**, 413 (1999).

[41] T. H. Pulliam and J. A. Vastano, Transition to chaos in an open unforced 2D flow, J. Comput. Phys. **105**, 133 (1993).

[42] W. Pfenniger, Transition in the inlet length of tubes at high Reynolds numbers, in *Boundary Layer and Flow Control*, Vol. 1, edited by G. V. Lachmann (Pergamon, New York, 1961), pp. 970–980.

[43] F. Daviaud, J. Hegseth, and P. Bergé, Subcritical Transition to Turbulence in Plane Couette Flow, Phys. Rev. Lett. **69**, 2511 (1992).

[44] C. H. K. Williamson, Oblique and parallel modes of vortex shedding in the wake of a circular cylinder at low Reynolds numbers, J. Fluid Mech. **206**, 579 (1989).

[45] C. H. K. Williamson and A. Roshko, Vortex formation in the wake of an oscillating cylinder, J. Fluids Struct. **2**, 355 (1988).

[46] J. S. Leontini, M. C. Thompson, and K. Hourigan, Three-dimensional transition in the wake of a transversely oscillating cylinder, J. Fluid Mech. **577**, 79 (2007).